Physics – Uspekhi **57** (11) 1099 – 1117 (2014)

INSTRUMENTS AND METHODS OF INVESTIGATION

PACS numbers: **07.85. – m**, **41.50. + h**, 61.05.cp

X-ray crystal interferometers

V V Lider

DOI: 10.3367/UFNe.0184.201411e.1217

Contents

1. Introduction **1099**
2. Moiré pattern phenomenon **1099**
3. Bicrystal interferometer **1100**
4. Two-beam and three-beam interferometers **1101**
5. Three-crystal Laue interferometer (LLL-interferometer) **1104**
5.1 Theory of LLL-interferometer; 5.2 Application of LLL-interferometer
6. Michelson X-ray interferometers **1113**
7. Conclusions **1115**
References **1116**

Abstract. Various configurations of the X-ray crystal interferometer are reviewed. The interferometer applications considered include metrology, the measurement of fundamental physical constants, the study of weakly absorbing phase objects, time-resolved diagnostics, the determination of hard X-ray beam parameters, and the characterization of structural defects in the context of developing an X-ray Michelson interferometer. The three-crystal Laue interferometer (LLL-interferometer), its design, and the experimental opportunities it offers are given particular attention.

1. Introduction

X-ray interferometry represents a relatively new field of modern experimental physics. Since its appearance 50 years ago in 1965, the technique has demonstrated unique capabilities in different fields of condensed matter studies, including measurements of fundamental physical constants, optical constants in hard X-rays (10–100 keV), precision measurements of the crystal lattice parameter, studies of structural defects in almost perfect single crystals, and X-ray phase-contrast microscopy.

Over a period of seven months in 1965, four papers were published in *Applied Physics Letters* that opened up the X-ray interferometry era. Two of them, which were published two weeks apart in October 1965, first demonstrated the possibility of obtaining X-ray moiré fringes from X-ray diffraction by a bicrystal in the cases when the interplanar spacings or orientations of its components differ insignificantly in a semiconducting heterostructure [1] or in a quartz crystal separated by an artificial crack [2].

In papers by Bonse and Hart [3, 4] published in April and August 1965, a three-crystal X-ray interferometer was designed and tested, which is capable of changing the phase difference of interfering beams. The introduction of a sample under study in one of two coherent X-ray beams produced by the interferometer leads to its phase change, which alters the result of interference with another (reference) beam.

Later on, Hart showed in paper [5] that such an interferometer can serve as an 'angström ruler', thus initiating its successful usage in metrology.

Features and the potential of the X-ray interferometry are discussed in several reviews [6–14]. They analyze the theory of X-ray interferometers [6–8, 10–12], their design [7–10, 12], the application in dispersion spectroscopy [7–10], the crystal lattice parameter determination [6–8, 13], structural defect studies [6–8, 10, 11], and phase-contrast microscopy [8–10, 13, 14]. Only in review [8], published by M Hart long ago in 1975, were all these applications discussed. In addition, such fields as bicrystal interferometers, X-ray Michelson interferometers, and nuclear resonance scattering have not been reviewed in detail.

The present review attempts to describe all possible lines of inquiry paved by the X-ray crystal interferometry, which are discussed in the scientific literature.

2. Moiré pattern phenomenon

X-ray interferometry is based on the moiré pattern. As is well known, moiré fringes arise when two linearly periodic structures are overlaid. The phenomenon happens when repeating elements of the two structures follow with slightly different frequencies and either are periodically superimposed or form pale gaps [15–17].

The moiré pattern appears as a linearly periodic picture with a period much larger than that of two overlaid structures. If the structures consist of a system of evenly spaced parallel planes with slightly different interplanar

V V Lider Shubnikov Institute of Crystallography,
Russian Academy of Sciences,
Leninskii prosp. 59, 119333 Moscow, Russian Federation
Tel. + 7 (499) 135 61 50
E-mail: lider@ns.crys.ras.ru; vallider@yandex.ru

Received 28 October 2013, revised 20 December 2013
Uspekhi Fizicheskikh Nauk **184** (11) 1217 – 1236 (2014)
DOI: 10.3367/UFNr.0184.201411e.1217
Translated by K A Postnov; edited by A Radzig

spacings d_1 and d_2, the moiré pattern arises with a period

$$\Lambda_x = \frac{d_1 d_2}{|d_1 - d_2|}\,, \tag{1}$$

called the dilatation moiré pattern (Fig. 1b). If systems of planes with the same period d are turned around with respect to each other through a small angle ε, the rotational moiré pattern arises with a period

$$\Lambda_y = \frac{d}{\varepsilon} \tag{2}$$

(see Fig. 1a) [16, 17]. In a mixed moiré pattern (Fig. 1c), the pattern period Λ_{xy} and the angle β between the moiré fringes and the x-axis normal to planes are given by the formulas [15, 16]

$$\Lambda_{xy} = \left[\Lambda_x^{-2} + \Lambda_y^{-2}\right]^{-1/2} = d_1\left[\frac{(d_1 - d_2)^2}{d_2^2} + \varepsilon^2\right]^{-1/2}, \tag{3}$$

$$\tan\beta \approx \frac{\Lambda_y}{\Lambda_x}\,, \tag{4}$$

respectively.

Formula (2) implies that the dilatation moiré fringes are parallel to the direction of the planes, while those of the rotational moiré pattern are perpendicular to it (see Fig. 1a, b).

In addition, there is translational moiré pattern: when structures with $d_1 = d_2 = d$ and $\varepsilon = 0$ are displaced with respect to each other in the direction normal to their planes, it is possible to detect a periodic (sine-like with a period d) change in the transmitted radiation intensity [17].

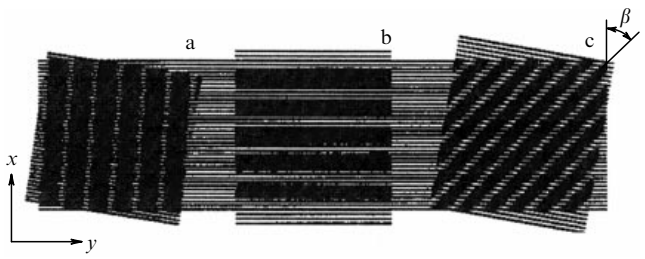

Figure 1. Schematics of rotational (a), dilatation (b), and mixed moirés [15].

The moiré pattern phenomenon in visible light has been known for a long time and has been widely exploited in science and technology. A small wavelength comparable to the crystal lattice period and high penetration ability make X-rays very promising for obtaining moiré patterns. The X-ray moiré pattern method became very popular in different studies (in particular, in the physics of crystals) due to its high sensitivity to small lattice deformations. Assuming a maximum permissible moiré fringe interval equal to one centimeter, for $d \approx 1$ Å from formulas (1) and (2) we find that the minimum detectable dilatation and rotation angles are 10^{-8} and 10^{-2} arcsec, respectively.

3. Bicrystal interferometer

Let us consider a crystal separated into two plane-parallel blocks *1* and *2* (Fig. 2a) by a boundary (stacking fault, crack) or by a nondiffracting gap (aerial or filled with some foreign material). When the angle of incidence of the primary narrow-front spherical X-ray wave on the reflecting plane is exactly equal to the Bragg angle, whose track segment is marked by DB, two waves originate at the block *1* exit: a transmitted one, and a diffracted one. The superposition of these two coherent waves forms the field of a standing wave with period d not only inside block *1* (triangle ACD), but also outside it (triangle ABC) [16]. In block *2*, the standing wave 'grid' consisting of antinodes and nodes is overlaid with its crystal lattice. As a result, two moiré patterns can be observed at the output: the bright field (in the transmitted beam O), and the dark field (in the diffracted beam H) images [17].

A theory of diffraction of a spherical wave by a bicrystal with a plane narrow aerial gap was elaborated in papers [18, 19], and the authors of Ref. [20] analyzed the moiré pattern due to the Laue and Bragg diffractions. Simon and Authier [21] developed a theory of X-ray moiré using Takagi equations. Paper [22] reported results of theoretical studies of X-ray diffraction in an interferometer in which blocks had equal interplanar spacings and there was a nondiffracting region between blocks, as well as diffraction in an interferometer in which blocks had different interplanar spacings but there was no nondiffracting region between the crystals. As was shown in the plane-wave approximation, the output intensity oscillation in interferometers of the first type should not be observed, but it necessarily arises in interferometers of the second type as a moiré pattern.

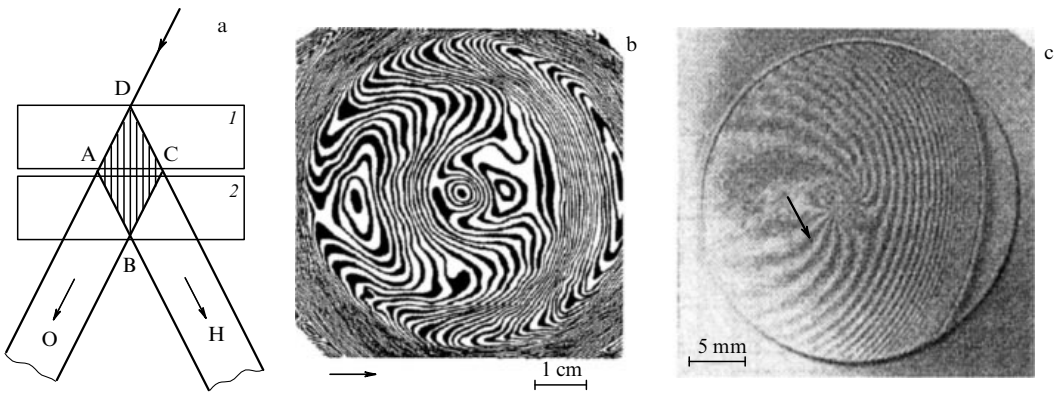

Figure 2. Schematics of X-ray moiré formation by bicrystals (a); moiré pattern from a silicon crystal implanted with oxygen (SIMOX) in the Bragg geometry (for convenience, the topogram contrast was artificially enhanced), reflection (224), $\lambda = 1.5$ Å [31] (b); interference fringes from a silicon crystal implanted with N^+ ions in the Laue geometry, reflection (111), MoKα radiation [25] (c); arrows indicate the directions of diffraction vectors (see text).

In the case of a spherical wave, at the output of type I interferometers, so-called translational fringes emerge [18] with a period Λ_g depending on the size t_g of the nondiffracting gap, the block thicknesses t_1 and t_2, and the extinction depth Δ_0 [23]:

$$\Lambda_g = \frac{\Delta_0}{t_g}\,(t_1 + t_2)\,\tan\theta_B\,, \qquad (5)$$

where θ_B is the Bragg angle, and $\Delta_0 = \lambda\left(\gamma_e|\gamma_i|\right)^{1/2}/C|\chi_{hr}|$ [18] (λ is the radiation wavelength, C is the polarization factor, χ_{hr} is the structure factor of the reflection, and γ_i and γ_e are the direction cosines of the incident and diffracted X-rays, respectively).

The authors of Ref. [24] theoretically predicted that when the angular divergence of the incident beam decreases, the value of Λ_g increases.

Experimentally, translational fringes were observed, for example, in X-ray diffraction by silicon implanted with high-energy ions [25], as well as by the $Si/Ge_xSi_{1-x}/Si$ heterostructure [26].

At the output of type II interferometers, the moiré fringes arise with spacing for the most part in good agreement with formulas (1)–(4). For example, papers [2] and [27] reported that the mutual misorientation of two parts of the crystals studied, caused by a crack, is 2 and 0.6 arcsec, respectively. Papers [1, 28] studied the mismatch of crystal lattices separated by a heteroboundary using the Bragg [1] and Laue [28] diffractions.

The implantation of a crystal with high-energy particles frequently leads not only to the formation of an amorphous layer at some depth but also to the formation of defects in a near-surface layer. In this case, it is possible to talk about a type III (symbiotic) bicrystal interferometer. Such an interferometer was theoretically considered in paper [20]. Paper [29] demonstrated both the theoretical and experimental dependences of the moiré pattern period on the sign of inconsistency of interplanar spacings of the bicrystal blocks, thus showing that formula (1) is not valid all the time. Paper [21] studied the bombardment of silicon by alpha-particles. The authors of papers [30, 31] tried to determine the strain tensor of the near-surface layer of a silicon sample implanted with oxygen ions with a subsequent annealing. To this end, a series of projective topograms of the studied sample was obtained using symmetric and asymmetric linearly independent Laue [30] and Bragg [31] reflections (one of the topograms is displayed in Fig. 2b).

In general, the interference pattern due to X-ray diffraction by a bicrystal can have a complex structure, which does not always allow a straightforward interpretation [25, 32, 33]. Figure 2c shows the projection topogram of a silicon crystal that demonstrates the 'transition' of translational fringes (the right panel of the topogram), which formed in the lenslike amorphous region made up due to nitrogen ion implantation, into moiré fringes (the left panel of the topogram), which arose due to strain fields of the second phase inclusion [25]. On the topogram, the diffraction vector (marked with the arrow) is perpendicular to the moiré fringes, which suggests the dilatation character of the deformation.

The fringes in the X-ray image can be interpreted as (1) fringes of equal thickness (*pendellösung* fringes) [34], (2) interference translational fringes which appear due to X-ray diffraction by a perfect bicrystal containing a diffraction-free zone between its two parts, or (3) a moiré pattern produced by two overlaid crystal lattices which have slightly

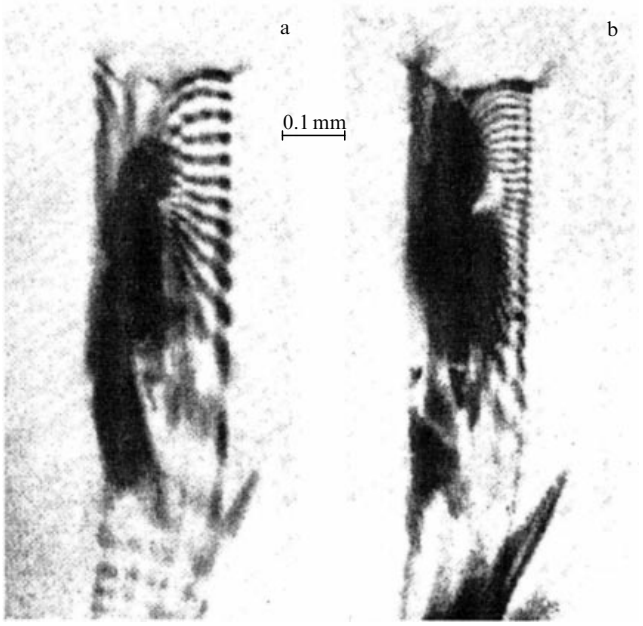

Figure 3. Moiré patterns on sectional topograms of a quartz crystal with a crack (upper part of the figure); MoKα radiation, reflection $(10\bar{1}0)$ (a) and $(20\bar{2}0)$ (b) [2].

different parameters and/or orientations. Considering the first possibility, we note that the spacing between fringes of equal thickness depends on the extinction length (hence, on the wavelength of the incident X-ray beam). For the second variant, there is the following rule: taking the opposite sign of the diffraction vector always leads to contrast inversion [35]. For the moiré pattern, as follows from formula (1), there are two criteria: the interfringe spacing does not depend on the X-ray wavelength, and it is inversely proportional to the order of reflection (Fig. 3).

In order to study the dislocation structure of natural quartz, Lang [36] utilized a 'reference' perfect quartz crystal superimposed on the sample under study in such a way that both crystals were simultaneously in the reflecting position (the authors of paper [37] described a simplified way of precision mutual adjustment of a crystal pair). The Burgers vector **b** of the dislocation can be determined by the formula $N = [\mathbf{g} \times \mathbf{b}]$, where **g** is the diffraction vector, and N is the number of additional moiré fringes observed at points A, B, C, D and E, which mark dislocation exits at the crystal surface (Fig. 4). Inspection of Fig. 4a suggests that $N = 2$ and $N = 4$ for the pair of A and B dislocations, and for dislocations C, D, and E, the cross product $[\mathbf{g} \times \mathbf{b}]$ is equal to 6, 3, and 4, respectively.

4. Two-beam and three-beam interferometers

The construction of the bicrystal interferometer considered above does not allow the experimentalist to change the phase relations of interfering coherent beams due to the small size (or the total absence) of the gap between the blocks. The presence of such a gap enables the phase change of one of the coherent beams by inserting into it the sample studied, a weakly absorbing plate (the phase modulator) or a wedge to produce the phase gradient.

In a two-beam interferometer, the primary X-ray beam breaks down spatially by the splitter S (Fig. 5a) into two

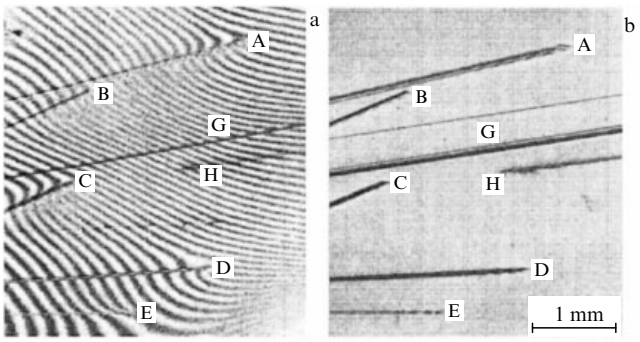

Figure 4. Moiré pattern produced from a bicrystal formed by dislocation and perfect natural quartz crystals (a); X-ray projection topograph of dislocation quartz (b). Reflection $(10\bar{1}1)$, MoKα radiation [36] (see text).

coherent beams that pass different optical paths and then, after diffraction by the mirror M, bring them together at the analyzer A.

Coherence is one of the main parameters of the X-ray beam that determines its capability to participate in interference interactions. The transverse and longitudinal (temporal) coherences are distinguished. Transverse coherence means a strong correlation (fixed phase relation) between electromagnetic oscillations that are completed at the same instant of time in different points of the plane perpendicular to the wave propagation vector. Its value l_x can be estimated by the formula $l_x \approx \lambda/\omega$ (λ is the wavelength, and ω is the solid angle subtended by the source). Longitudinal coherence means a strong correlation between electromagnetic fields in one point but at different instants of times. Its value can be estimated as $\lambda^2/\Delta\lambda$, where $\Delta\lambda$ is the interferometer pass band.

Geometric conditions for the interference occurrence require the difference between the optical paths of two beams to be smaller than the longitudinal coherence length of interfering beams, i.e., the path difference of the beams to be smaller than a few dozen microns, and that the precision of the interferometer manufacturing be controlled by the same parameter.

X-ray interferometers, as a rule, are made of single-crystal silicon. The very high adjustment demands on the interferometer resulted in its monolithic construction. Silicon is chosen because it is an ideally fragile material at room temperature, it has a sufficiently low thermal expansion coefficient and high thermal conductivity, it has no mechanical hysteresis or fatigue, and elastic parts made of this material work perfectly. This makes silicon an extremely useful material in electrotechnology, electronics, and mechanical and optical engineering related to the design of machines, tools, and other devices with extremely demanding limits, good reproducibility, and long-term stability. Due to very good scattering power and low absorption of X-rays, silicon is a very suitable material for X-ray diffractometry. It is easily shaped mechanically and is virtually free of impurities, and defect-free crystal rods with sufficiently high diameters and specific crystallographic orientations are easily available. From a crystal boule a diamond drill cuts a configuration consisting of three or more vertical wafers (lamellae) on the common crystal base. For many semiconductors, such an operation leads to the formation of a layer of the damaged material several dozen micrometers in thickness. This damaged layer can be easily removed by chemical polishing (for example, by a mixture of HF and HNO for silicon and germanium) [7].

Such interferometers are characterized by the presence of a so-called interference loop consisting of two 'branches' (trajectories).

In principle, each diffraction optical element can operate for both reflection (in the case of Bragg diffraction) and transmission (in the case of Laue diffraction). In the interferometer, each of the two separate trajectories usually includes a certain sequence of reflections, which are usually specially abbreviated. For example, in the interferometer marked with the sequence of Roman characters LBL, Laue diffraction occurs in the first and third optical elements, and Bragg diffraction occurs in the second optical element.

Figure 5 shows four perspective layouts of a two-beam interferometer [38]. The three-beam Laue interferometer (LLL) (Fig. 5a) is the most frequently used; its features and experimental capabilities are considered in detail below. The LLL-interferometer [39] provides the crossing of coherent beams (the central circle in Fig. 5b) in free space, which allows originating of a standing wave suitable for studies of a broad range of objects. In addition, the presence of several interference loops broadens the functional capabilities of such an interferometer [40].

However, the Laue transmission geometry has several shortcomings: (1) loss of intensity due to absorption in each lamella; (2) 50% loss of intensity due to the presence of unused beams during diffraction by the mirror (Fig. 5a), and (3) decrease in the spatial resolution due to the X-ray filling of the entire Borman triangle in the analyzer. These defects (all or some of them) can be overcome applying Bragg reflection.

The BBB-interferometer (Fig. 5c) [41–43] uses Bragg splitting of the beam by a very thin crystal. Its design is

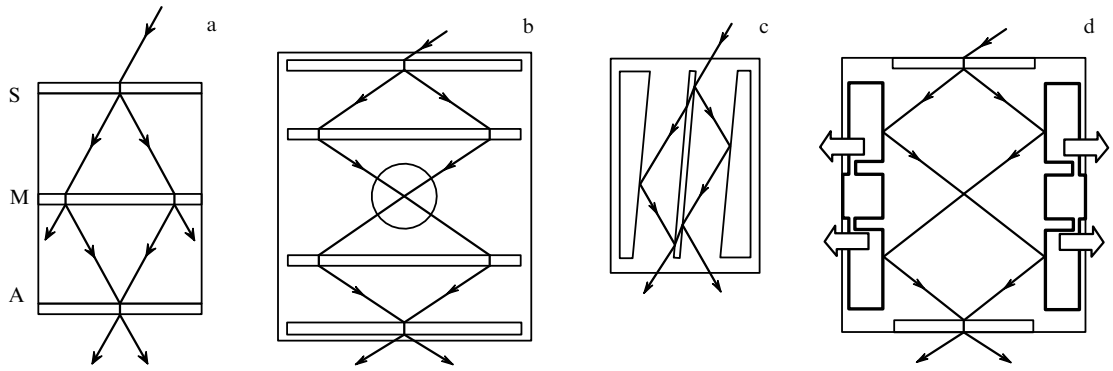

Figure 5. Optical layouts of two-beam (a) LLL-, (b) LLLL-, (c) BBB-, and (d) LBBL-interferometers (see text).

based on the fact that when the Bragg condition is not precisely fulfilled for a primary beam, both a diffracted beam and a secondary transmitted beam of almost equal intensity exist, which can be further used for interference. The choice of the right angle of incidence can be 'done' by the interferometer itself when illuminating it by a divergent primary beam. Taking into account that the energy of weakly absorbable wave fields propagates almost along the reflecting planes, BBB-interferometers are cut for 'oblique' (asymmetric) reflections that shorten the path of X-rays in the crystal. In paper [44], a BBB-interferometer was applied to obtain phase-contrast images, while in papers [45, 46] such an interferometer was utilized as an analog of the Michelson optical interferometer.

Mixed LBL- and BLB-interferometers (not shown in Fig. 5) were discussed in paper [42]. At least some arguments in favor of mixed optical components are reduced to the statement that in most practical situations Bragg-mirrors provide a higher intensity than their Laue 'competitors', whereas Laue-splitters, as a rule, are more effective than Bragg-splitters due to a shorter X-ray path inside the crystal [7].

For a number of reasons, the LBL-geometry is more advantageous than the BLB-geometry: a BLB-interferometer has a small field of view and low intensity of an interference pattern due to higher X-ray absorption losses. As manufacturing the ideal interferometer is impossible, even a small deviation from a strictly symmetric geometry will decrease the moiré pattern contrast. While the necessary geometrical requirements for the orientation of the working surfaces of units of LBL- and BLB-interferometers are rather high, they are significantly decreased in an LBBL-interferometer (Fig. 5d) due to double X-ray reflection from each of the mirrors [42].

The exploitation of mixed type interferometers is significantly complicated because, due to the refraction effect, the Bragg angle in the Laue geometry differs from the angle in the case of Bragg diffraction: the refraction correction is proportional to $1 + b$, where b is the asymmetry coefficient [34], which is positive or negative for Bragg and Laue diffractions, respectively.

This can lead to unacceptable intensity losses. In paper [47], the necessary corrections were proposed to introduce using small elastic strains of the mirror walls of the interferometer in the directions indicated in Fig. 5d by arrows.

Returning to the two-beam BBB-interferometer, we note that its construction allows the intensity losses due to beam diffraction by the mirrors to be avoided, but the Bragg-splitter is rather ineffective since it absorbs X-rays and enhances the beam fronts.

Graeff and Bonse [48] proposed the construction of a three-beam BBBB-interferometer. The main idea of such a device consists in the simultaneous excitation of two [Si (440) and Si (404)] reflections in the Bragg geometry to split the primary beam into two coherent ones and their subsequent interference after four Bragg reflections using the same pair of reflections (Fig. 6a). Here, one half of the beam intensity is lost during the second Bragg reflection, and the other half is lost during the third Bragg reflection.

It should be noted that in this interferometer the splitting of the primary wave amplitude (and not of its front) occurs, unlike in other types of interferometers; therefore, here the functionality of the interferometer is not limited by the longitudinal coherence of the radiation.

Paper [49] describes the construction of a three-beam BBB-interferometer (Fig. 6b), including reflecting planes $(10\bar{1})$, $(1\bar{1}0)$ of the beam splitter S and the analyzer A, as well as planes $(01\bar{1})$ of the mirrors M1, M2. Reducing the number of mirrors to two (instead of four in the BBBB-interferometer) pursues the object of decreasing the X-ray absorption.

The described constructions of three-beam interferometers are based on coplanar multiwave diffraction, when the normals to the reflecting planes and the primary beam lie in one plane. If this condition is not met, the multiwave diffraction is called noncoplanar.

When using the multiwave coplanar diffraction, an interferometer can work only at a certain wavelength, and its spectral transmission band is very narrow compared to a dispersion-free two-beam interferometer. This makes the exploitation of the interferometer relatively difficult and demands high quality of crystals and interferometer manufacturing.

In the constructions of three-beam interferometers described above, the choice of the reflecting planes and the corresponding reflections was dictated by the possibility of experimentally realizing the multiwave coplanar diffraction in laboratory conditions using the spectral line $NiK\alpha_2$. For phase-contrast experiments with a BBBB-interferometer, the authors of paper [51] utilized synchrotron radiation (SR): for the pair of reflections Si(440)/Si(404)), the primary beam energy was $E = 7.46$ keV; for Si(880)/Si(808), the energy was $E = 14.91$ keV.

There are no strict selection rules limiting the radiation wavelength to realize multiwave noncoplanar diffraction, which is advantageous. Paper [50] reported obtaining of phase-contrast images of a plastic sphere with good resolu-

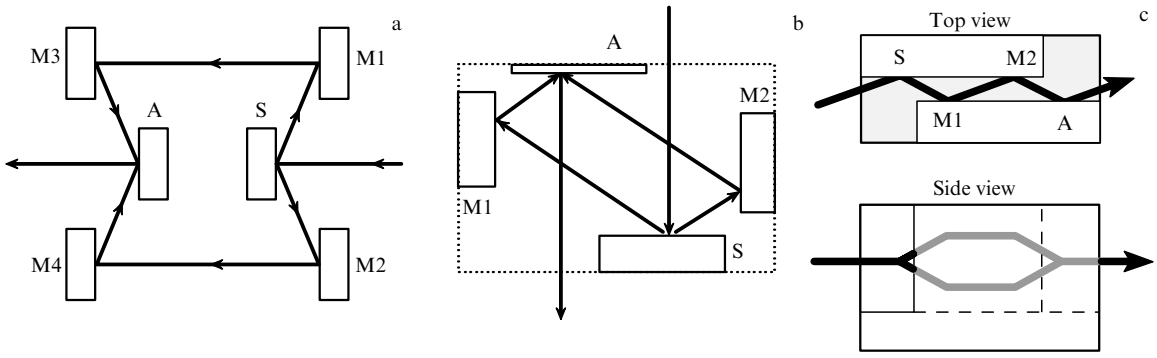

Figure 6. Optical layouts of three-beam interferometers: coplanar (s) BBBB- and (b) BBB-interferometers [48, 49]; (c) noncoplanar BBBB-interferometer [50]: S — beam splitter, M1, ..., M4 — mirrors, and A — analyzer.

tion using a three-beam two-block BBBB-interferometer with parallel working planes and noncoplanar multiwave diffraction (Fig. 6c) with reflections (311) and $(3\bar{1}\bar{1})$ and the radiation energy $E = 10.3$ keV.

5. Three-crystal Laue interferometer (LLL-interferometer)

The most widely used interferometer is the so-called three-crystal Laue dispersionless interferometer (LLL-interferometer), in which the coherent splitting of the primary beam and the convergence and superposition of the resulting beams are made by consecutive Laue-diffractions (Fig. 7).

5.1 Theory of LLL-interferometer

By applying the plane-wave theory, Bonse and Hart [52] were the first to propose in 1965 the principles of a strongly absorbing LLL-interferometer. Later on, the authors of paper [53] developed a theory of a symmetric LLL-interferometer in the presence of arbitrary absorption for plane and spherical waves and estimated manufacturing errors on the output beam profile intensity. The spherical wave diffraction was considered in papers [54, 55], and the case of a polychromatic divergent primary beam was studied in Ref. [56]. The effects caused by deviations from the ideal interferometer geometry were first investigated by Bonse and te Kaat [57]. Output beam front narrowing due to dynamical focusing of X-rays under the certain choice of the crystal plate thicknesses was analyzed by Trouni and Arutyunyan [58].

When no sample is inserted into one of the interfering beams, the topogram is homogeneous and does not contain the moiré fringes if the interferometer is ideally manufactured, i.e., when the crystal wafers S, M, and A are exactly parallel to each other, and have the same thickness and spacing. In this case, the interferometer is thought to be ideally focused. The insertion of a phase object (Fig. 7a) distorts the beam wave front, which may cause a moiré pattern to appear in the topogram.

To study bulky objects or samples put in special chambers to investigate external effects, a skew-symmetric variant of the LLL-interferometer is frequently used (Fig. 7b).

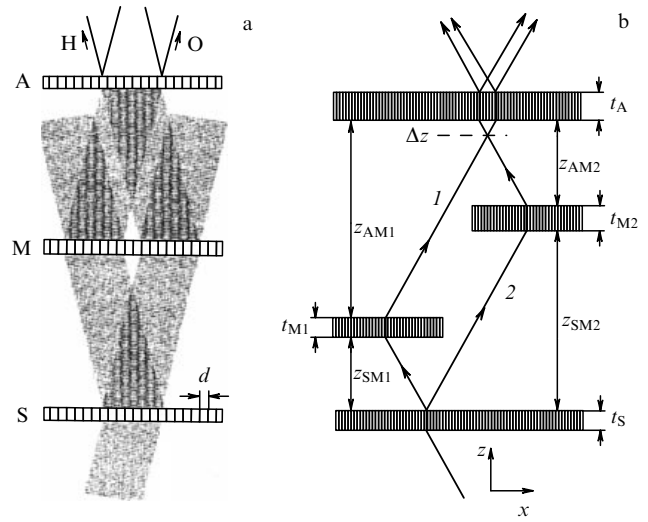

Figure 7. Optical layouts of LLL-interferometer: (a) symmetric [6], and (b) skew-symmetric [59] (see text).

The optimal contrast of the moiré pattern is achieved under certain geometrical conditions [54, 57, 59]. The key property is so-called zero defocusing, Δz (Fig. 7b):

$$\Delta z = \frac{z_{AM1} + z_{AM2} - z_{SM1} - z_{SM2}}{2}\,, \tag{6}$$

where z_{AM1}, z_{AM2}, z_{SM1}, z_{SM2} are distances between the analyzer and mirror M1, the analyzer and mirror M2, the beam splitter and mirror M1, and the beam splitter and mirror M2, respectively.

In addition, the phase homogeneity will be preserved provided that the thicknesses of all three crystal lamellae are the same:

$$t_{M1} = t_{M2} = t_M = t_S = t_A\,. \tag{7}$$

Theoretical calculations of spherical wave diffraction in a nonabsorbing LLL-interferometer showed [54] that, despite the thickness control of crystal wafers and their spacings, it is virtually impossible to construct an instrument with a sufficient contrast of the moiré fringes. The LLL-interferometer with a crystal-mirror thickness equal to the double thickness of the beam-splitter and analyzer ($t_M = 2t_S = 2t_A$) is the most promising instrument. In the last case, X-ray focusing on the output analyzer lamella can be observed.

A detailed analysis of the defocusing effect on the visibility (contrast) of the fringe pattern can be found in paper [57].

When two coherent beams with amplitudes A_1 and A_2 and phase difference Φ interfere, the observed intensity is given by the formula

$$I_0 = A_1^2 + A_2^2 + 2A_1A_2|\gamma|\cos\Phi\,, \tag{8}$$

where γ is the coherence function. For a pointlike radiation source, the interference pattern visibility V, which is determined as the ratio of the intensity oscillation amplitude to its mean value, is given by the expression

$$V = \frac{I_{max} - I_{min}}{I_{max} + I_{min}} = \frac{2p}{1+p^2}\,|\gamma|\,. \tag{9}$$

Here, $p = A_1/A_2$, $\gamma = \sin w/w$, $w = 2\pi|\Delta z||\tan\varepsilon_m|/\Delta_0\tan\theta_B$, where $2\varepsilon_m$ is the angle interval inside which the X-ray wave propagates in the crystal. For a finite-size source, in the diffraction plane one has

$$V = \frac{2p}{1+p^2}\left|\frac{1}{w}\sin\left[w\left(1 - \frac{|\Delta z|\tan\theta_B}{T|\tan\varepsilon_m|}\right)\right]\right|, \tag{10}$$

where T is the total thickness of lamellae S, M, and A ($T = t_S + t_M + t_A$).

An analysis of formula (10) suggests that in weakly absorbing interferometers the defocusing effect reduces the visibility more strongly than in highly absorbing crystals, since $p \approx 1$ for the latter [17].

As $|\Delta z|\tan\theta_B \geqslant T|\tan\varepsilon_m|$, the coherence is completely lost. For the interferometer used in one of the experiments [57], $T = 831$ μm, and $|\tan\varepsilon_m| = 0.136$ for CuKα radiation and reflection Si(220). With these values in mind, $V = 0$ at $|\Delta z| = 258$ μm, whereas the contrast disappeared already at $|\Delta z| \approx 25$ μm, which implies that in this case the interference pattern visibility is determined by the ratio $\sin w/w$. This example suggests that, in order to provide a good contrast of the moiré fringes, the parts of the interferometer should be manufactured with a micron accuracy [7].

During spherical wave diffraction in a perfect interferometer with a fixed defocusing Δz, the phase picture represents a collection of equally spaced lines perpendicular to the scattering plane [53, 57]. The distance between the defocusing fringes $\Lambda_{\Delta z}$ is given by the formula

$$\Lambda_{\Delta z} = \frac{T\Delta_0 \tan\theta_B}{\Delta z} . \quad (11)$$

A comparison of formulas (11) and (5) shows that the defocusing changes the phase in a way similar to the diffractionless zone of a bicrystal. Here, if the lattice parameter of the analyzer crystal differs from that of the beam splitter and mirror crystals, the expression for the determination of the periodicity of the dilatation moiré pattern Λ_x takes the form [60]

$$\Lambda'_x = \frac{\Lambda_x \Lambda_{\Delta z}}{\Lambda_x \pm \Lambda_{\Delta z}} . \quad (12)$$

If only lattice rotations are used in the analyzer crystal of an interferometer, then purely rotational moiré fringes are formed in the topogram, which are inclined to the x-axis by angle β [see Fig. 1 and Eqn (4)]:

$$\pm\tan\beta \approx \frac{\Lambda_y}{\Lambda_{\Delta z}} . \quad (13)$$

Thus, using the defocusing fringes, it is possible to determine the form and amplitude of the crystal lattice deformation. In addition, from the sign of the inclination angle of the fine structure of fringes, it is possible to infer the direction of rotation of the reflecting planes in the interferometer analyzer crystal.

Paper [61] reported that when two coherent beams are superimposed in an X-ray symmetric interferometer with a steplike mirror block, fringes due to defocusing and different thicknesses arise. When the prerequisites exist to appearing such fringes simultaneously with the moiré fringes, the moiré pattern method does not allow the unique determination of the amplitude and form of the crystal lattice deformation without taking into account the effects of defocusing and different thicknesses. However, using the radiation with different wavelengths and/or different reflection orders, it is possible to single out the 'structural' moiré pattern.

Presently, the following reasons for the appearance of the moiré pattern are recognized: the difference in the interplanar spacings and nonparallelism of reflecting planes of individual crystal-optic units of an interferometer, the nonparallelism of their enter and exit surfaces [62], the difference in their thicknesses, violation of conditions restricting distances between neighboring units, and, finally, the phase front inhomogeneity caused by the insertion of a sample into one of the interferometer loops [63]. The situation may arise, however, when the moiré fringes will not be observed in the presence of one or several above-mentioned causes. For example, assume that the beam splitter and analyzer are ideal crystals with the interplanar distance d_0, the crystal lattice of the mirror block M1 (Fig. 7b) has the interplanar distance d_1 and rotation angle ε_1, while the M2 lattice has the interplanar distance d_2 and rotation angle ε_2. Then, one obtains [64]

$$\Lambda = d_0\left[\left(\frac{\Delta d_2}{d_2} + \frac{\Delta d_1}{d_1}\right)^2 + d_0^2\left(\frac{\varepsilon_1}{d_1} + \frac{\varepsilon_2}{d_2}\right)^2\right]^{-1/2} , \quad (14)$$

where Λ is the distance between the moiré fringes, $\Delta d_1 = d_1 - d_0$, and $\Delta d_2 = d_2 - d_0$.

Formula (14) implies that, for example, at $\Delta d_2/d_2 = -\Delta d_1/d_1$ and $\varepsilon_1 = \varepsilon_2 = 0$, no moiré pattern should arise. On the other hand, the deformation effect of some units of an interferometer (arising, for example, during the crystal boule growing) in some cases can be compensated for by using the corresponding phase plates [65].

Various factors affecting the interference topogram, acting both separately and in different combinations, show how difficult a unique explanation of the moiré patterns could be. Apparently, it is quite easy to estimate the effect of a given factor on the interference pattern intensity in the absence of all the rest, but in real experiments several factors act 'consistently', which significantly complicates a unique interpretation of X-ray moiré patterns [63].

5.2 Applications of LLL-interferometer

5.1.1 Phase-contrast imaging. It is well known that when an X-ray wave passes through matter, both its absorption and a phase change occur. The phase shift due to the X-ray propagating through a sample of thickness T depends on the decrement δ of the X-ray refraction coefficient and is equal to $(2\pi/\lambda)\,\delta T$, while the absorption B is due to the intensity decrease: $\ln(I_0/I) = (4\pi/\lambda)\,BT$. Parameters δ and B determining the X-ray refraction coefficient n far from the absorption edges ($n = 1 - \delta + iB$) are described by the formulas [66]

$$\delta = \frac{\lambda^2 r_0 N_A Z}{2\pi} , \quad (15)$$

$$B = \frac{\mu\lambda}{4\pi} , \quad (16)$$

where N_A is the number of atoms per unit volume, r_0 is the classical radius of an electron, Z is the atomic number of the sample material, and μ is the linear X-ray absorption coefficient.

It is interesting to note that the parameter δ for soft tissues is much larger than B. The estimate of δ and B for biological tissues showed [67] that $\delta = 10^{-6} - 10^{-8}$ and is about 1000 times as high as B ($B = 10^{-9} - 10^{-11}$) for X-rays in the energy range 10 keV–50 keV. Therefore, the difference in the X-ray phase shift for tissues of various densities is much larger than in the linear absorption coefficients. Consequently, the phase-contrast image can significantly enhance the X-ray sensitivity to small changes in the structure of samples examined. The method is very effective for studies of weakly absorbing objects with small internal absorption coefficient variations, since variations of the absorption coefficient decrement δ in the objects are important. Therefore, it has found wide utility in biomedicine, for example, in angiography [68–70], oncology [71–73], and neurology [74, 75].

Information about the wave phase can be obtained applying the algorithm [76] developed for the phase step method [14, 77, 78]. The method consists in recording a series of interference patterns with a step-by-step changing of phase shifts. To change the relative phase between the upper and bottom beams, a phase modulator (Fig. 8a) — a plate turning around the axis normal to the beam propagation — is inserted into the bottom beam. The relative phase change depends on the effective plate thickness and its refraction coefficient.

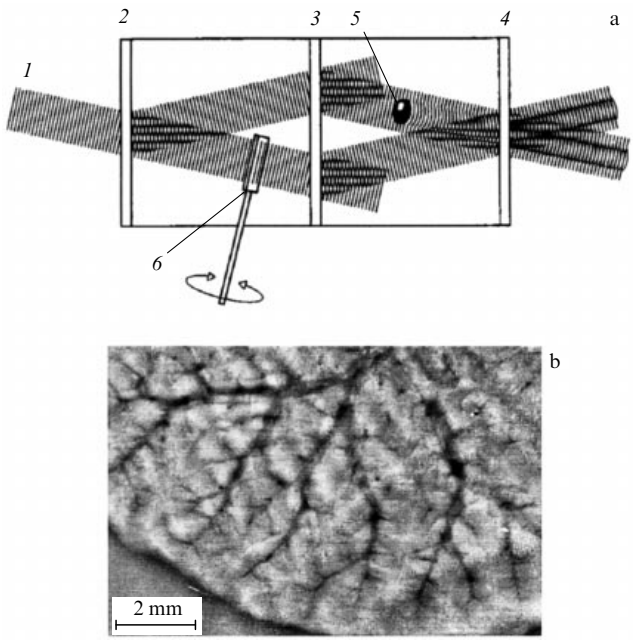

Figure 8. (a) Optical scheme of an LLL-interferometer: *1* — primary X-ray beam, *2* — beam splitter, *3* — mirror, *4* — analyzer, *5* — sample, and *6* — phase modulator [88]. (b) Phase-contrast image of blood vessels of a rat liver obtained by the phase step method [78].

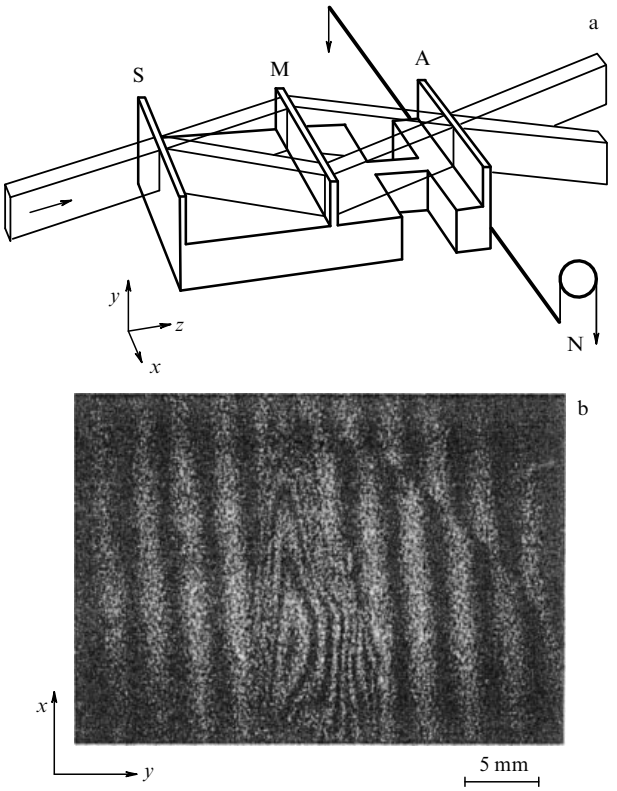

Figure 9. (a) Deformable interferometer in which the analyzer crystal (A) is joined with the beam splitter (S) and the mirror (M) by a thin elastic bar. (b) Phase-contrast image of an epoxy resin drop on the cover slip obtained using the X-ray rotational moiré (the round glass edge is seen on the top right) [82].

During each scan, the phase is shifted by $2\pi/J$ (J is an integer). At each step, the interference pattern is recorded repeatedly with no sample in the upper beam, yielding in total $2J$ images, from which the phase map can be restored using simple algebraic expressions. The number of images can be 8 ($J = 4$) or even more. Thus, the phase might be restored accurate to 2π. This uncertainty may be removed using the phase sweeping methods [79] if there are no phase jumps on the scales smaller than the resolution of the method.

The phase can be determined without necessary analysis of several data sets applying the Fourier transform method [14, 80]. Experimentally, in this method the phase modulator is replaced by a wedgelike plate. By choosing the material of the wedge, its angle α, and the X-ray wavelength, it is possible to produce the basic dilatation moiré pattern consisting of equally spaced interference fringes with a given interval d_M: $d_M = \lambda/\delta \tan\alpha$ [34]. From distortion of these fringes caused by the presence of a sample under investigation, it is possible to restore the phase map of the sample [81].

Another way of producing the basic moiré pattern consists in using a deformable interferometer, in which the analyzer crystal is connected to the interferometer base by only a thin elastic bar [65, 82]. Turning around the interferometer longitudinal axis (the z-axis) leads to the formation of the rotational moiré pattern (Fig. 9).

The phase-contrast image of the entire sample under investigation can be obtained when the sample is 'bathed' in the beam. If the beam lateral size in the diffraction plane is smaller than the sample size, there are two possible ways to solve the problem: (1) to increase the beam size by using an asymmetrically cut pre-monochromator (Fig. 10a) or an asymmetric reflection of the interferometer [7]; (2) to scan the interferometer and the detector as a whole in the interval corresponding to the sample size [7] (Fig. 10b).

The resolution of the method may be restricted by the detector resolution. It is also restricted by the X-ray trajectory

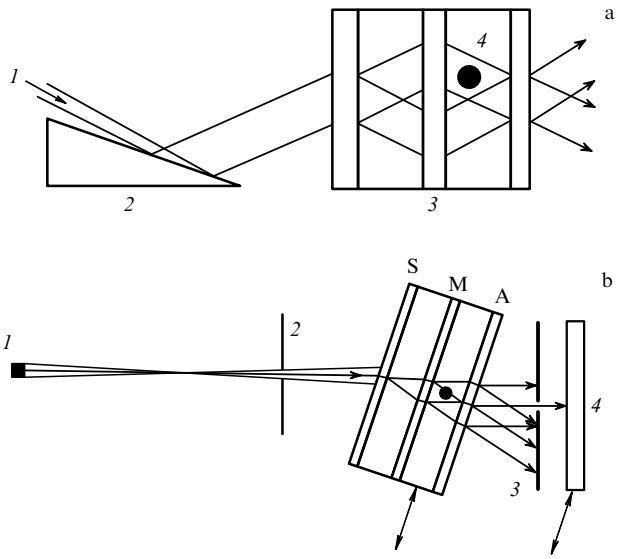

Figure 10. Optical schemes of the sample imaging: (a) *1* — primary X-ray beam, *2* — preliminary asymmetric monochromator, *3* — interferometer, *4* — sample, and (b) *1* — X-ray source, *2* and *3* — fixed slits, *4* — detector being scanned synchronously with interferometer (S, M, A — beam splitter, mirror, and analyzer, respectively) [7].

divergence within the double Bragg angle when passing through the analyzer crystal [34] and can be as high as $2T \tan\theta_B$ (T is the crystal thickness). One way to improve the resolution is to decrease the analyzer lamella thickness [83], although this should be done with care due to the possible

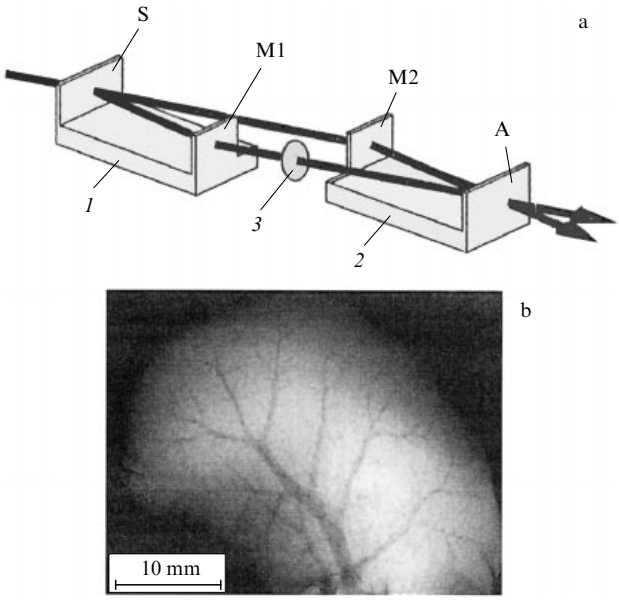

Figure 11. (a) Optical scheme of a separated type LLL-interferometer: *1* and *2* — silicon crystal blocks with beam splitter S/mirror M1 and mirror M2/analyzer A, and *3* — sample. (b) Phase-contrast image of blood vessels of a rat liver. The field of view is significantly larger than that shown in Fig. 8b due to the use of the separated type LLL-interferometer.

appearance of thickness oscillations. Another way consists in using a crystal interferometer with a Bragg analyzer [44].

The finite sizes of interferometers hamper studies of bulky samples. An attempt to increase the gap between the lamellae by enlarging the dimension of a single-crystal boule showed apparently that this is not a solution [84]. Paper [85] discussed the possibility of using a skew-symmetric interferometer consisting of two monoblocks to obtain phase-sensitive images (Fig. 11a). However, since the advantage of exploiting a monolithic configuration should be abandoned, so a high-precision adjustment of the interferometer units is required [86].

Several phase-contrast projections obtained for different angular positions of the sample can be joined mathematically for performing its tomography [87–89], which probes the internal and external structure of the sample without its destruction.

5.2.2 Measurement of anomalous dispersion. X-ray interferometry is one of the most precise methods for determining the anomalous dispersion of the atomic scattering factor $f = Z + f' + \mathrm{i}f''$. Moreover, interferometry allows simultaneous measuring of both f' and f''. Knowledge of the precise values of f' and f'' is necessary to determine the phase, and in some cases to decipher the crystal structure, as well as to study the structural properties of ions and molecules in condensed media.

For an ideally focused ($|\gamma| = 1$) X-ray interferometer with the insertion of a sample with thickness T into one of the interfering beams (for example, with the wave field amplitude A_2), formula (8) takes the form [90]

$$I_\mathrm{s} = A_1^2 + A_2^2 \exp(-\mu T) + 2A_1A_2 \exp\left(-\frac{\mu T}{2}\right) \cos\frac{2\pi T}{\lambda}\,\delta + \Phi\,. \qquad (17)$$

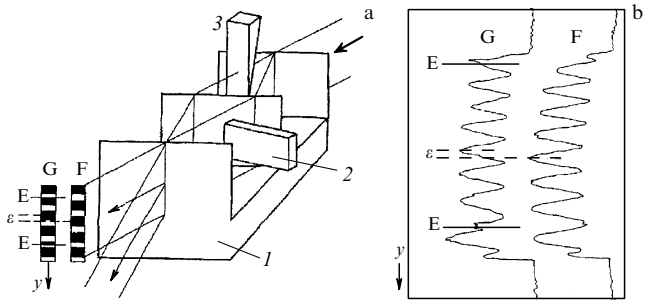

Figure 12. (a) Experimental setup for measuring anomalous dispersion: *1* — X-ray interferometer, *2* — sample, and *3* — wedge. (b) Densitometry of moiré fringes obtained from an LiF sample 1765 μm in thickness, MoKα radiation, reflection (220). Fringes obtained when the sample is inserted (scan G) are shifted by ε relative to the fringes obtained without the sample (scan F); region EE corresponds to the time during which the sample was in the beam [92].

Taking into consideration the anomalous dispersion, we arrive at

$$\delta = \frac{\lambda^2 r_0 N_\mathrm{A}(Z + f')}{2\pi}\,, \qquad (18)$$

$$B = \frac{\mu\lambda}{4\pi} = \frac{\lambda^2 r_0 N_\mathrm{A} f''}{2\pi}\,. \qquad (19)$$

Clearly, δ and, hence, f' might be determined from the phase shift produced by the sample, and f'' might be inferred from the change of the moiré fringe amplitude.

Different methods can be used to measure the phase shift [91]. In papers [92–95], a plastic wedge was inserted into one of the interfering beams (Fig. 12a) and thus produced a phase shift that varied linearly along the wedge height (i.e., the beam). Here, equally spaced moiré fringes appeared. The wedge remained intact during the experiment. The insertion of a plane-parallel sample into another beam led to a phase shift, which resulted in the moiré pattern shifting by a fraction ε of its period (Fig. 12b). Here, the phase shift caused by the sample is $2\pi(m + \varepsilon)$, where m is an integer [92, 93].

For changing the phase, the immobile wedge might be replaced by a plane-parallel plate (phase modulator) turning around the axis normal to the reflecting planes during the experiment. In papers [96, 97], for any chosen energy, the phase modulator rotation yielded two conjugate interference patterns of the translational moiré: one with the sample in the beam, the other without it. The conjugate curves were registered during alternating insertion of the sample into the beam and its removal at short time intervals.

5.2.3 Scanning interferometer. In the scanning interferometer [5, 90, 98–100], the translational moiré pattern is formed not due to the standing wave front shift relative to the immobile analyzer, as in the case of a phase modulator, but due to the analyzer displacement relative to the standing wave. The elasticity of silicon is utilized in such an interferometer, which is needed to provide a parallel and rectilinear displacement of one crystal unit of the interferometer relative to its immobile part. The interferometer is manufactured in such a way that its analyzer is attached to the silicon block that carries the beam splitter and mirror by a pair of thin silicon strips, as shown in Fig. 13a. The scanning interferometer provides excellent stability and no backlash when displaying the analyzer. However, the range of linear scanning is

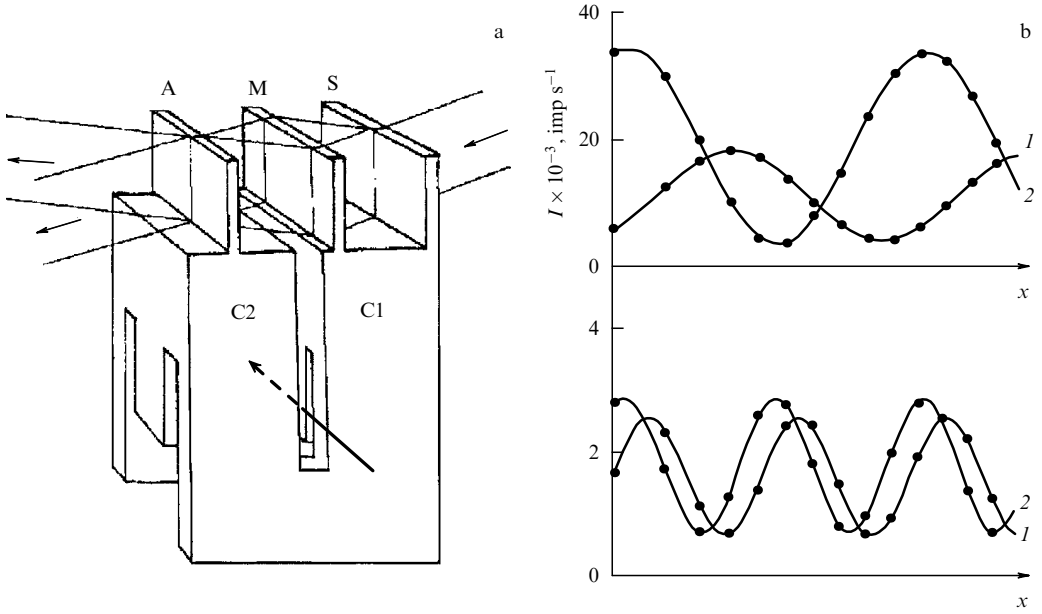

Figure 13. (a) Schematic of the Hart scanning interferometer [5, 7]: A — analyzer on the mobile part of the interferometer C2; S, M — beam splitter and mirror on its immobile part C1; the thick arrow marks the loading application area. (b) Change in the interference pattern intensity when scanning the analyzer along the diffraction vector (along the *x*-axis) for reflection (220) (the upper pair of curves) and reflection (440) (the bottom pair of curves) for the sample in the beam (curves *1*) and outside the beam (curves *2*) [99].

restricted by parasitic bendings and the elastic properties of the interferometer material [98].

Measurement of anomalous dispersion. The characteristic drawbacks in the methods considered in Section 5.2.2 are the distortion of the interference pattern, and a reduction of its contrast due to unwanted X-ray absorption by the phase plates. The scanning interferometer is free from this shortcoming.

The application of the scanning interferometer also allows avoidance of another defect, the difficulty of precise measurement of the thickness of the sample under study, which increases the error in the determination of the anomalous dispersion of the X-ray atomic scattering factor. The authors of papers [90, 96–100] managed to exclude the sample thickness from the determination of f' by using harmonics of the fundamental wavelength λ. If the harmonic with wavelength $\lambda/2$ dominates, then

$$(f')_\lambda = \frac{P}{2}\left[Z + (f')_{\lambda/2}\right] - Z, \tag{20}$$

where $P = p_\lambda / p_{\lambda/2}$, p is the phase shift. As $(f')_{\lambda/2} \approx 0.005Z$, the experimental results weakly depend on theoretical model calculations of quantity $(f')_{\lambda/2}$ [98]. To generate the harmonics, bremsstrahlung radiation from an X-ray tube [98] or SR [90, 95–97, 99, 100] was used. The X-ray energy was varied by changing the angular position of the pre-monochromator relative to the primary beam.

Figure 13b depicts the dependence of the interference pattern intensity as a function of the analyzer location for the fundamental wavelength [reflection (220)] and the $\lambda/2$ harmonic [reflection (440)] [99].

Measurement of lengths (*linear scanning*). The development of highly sensitive measurement tools, their calibration, and reference to absolute length standards are essential for length and (or) shift measurements and control. There are many sensors operating in the nanometer and subnanometer ranges: differential transformers, optical interferometers, capacitive sensors, and sounding microscopes. However, it is evident that none of them is capable for making its own precise calibration. For tiny displacements, it is impossible to predict the behavior of these devices due to their 'fine' features, such as hysteresis, nonlinearity, or instability. The X-ray interferometry, in which the silicon lattice parameter is used as the length standard, increased the sensitivity of the calibration method by at least two orders of magnitude [101].

If the lattice of the analyzer is displayed relative to the crystal lattice of the beam splitter, the intensity of radiation at the interferometer output should oscillate with a sine period corresponding to a displacement by one interplanar lattice spacing, which is 0.192 nm, when using silicon reflection (220). Counting the number of sine periods yields the analyzer shift with a subnanometer accuracy. Therefore, the X-ray interferometer can be considered as an 'angström ruler' or a precision object table, the steps or displacements of which are related to the silicon lattice parameter. In the first case, the interferometer can be used for calibrating the linear displacement sensors [101–104] and measuring the nonlinearity of an optical interferometer or encoder [105, 106]. In the second case, it can be utilized jointly with scanning tunneling [107–109] or atomic-force [110] microscopes. For above-mentioned applications, however, the construction of the Hart scanning interferometer (Fig. 13a) is inadequate due to a small scanning range of ~ 0.1 μm [5]. It has been possible to increase the analyzer displacement range to 10 μm by raising the sophistication of the construction of the scanning interferometer [109].

Measurement of angles (*angular scanning*). If in a skew-symmetric X-ray interferometer four lamellae are separated between two blocks (two lamellae in each) capable of rotating relative to each other in the diffraction plane (Fig. 14b), then theoretical and experimental studies [111–114] demonstrate that the output interferometer intensity will periodically vary depending on the relative angle formed by the blocks. The

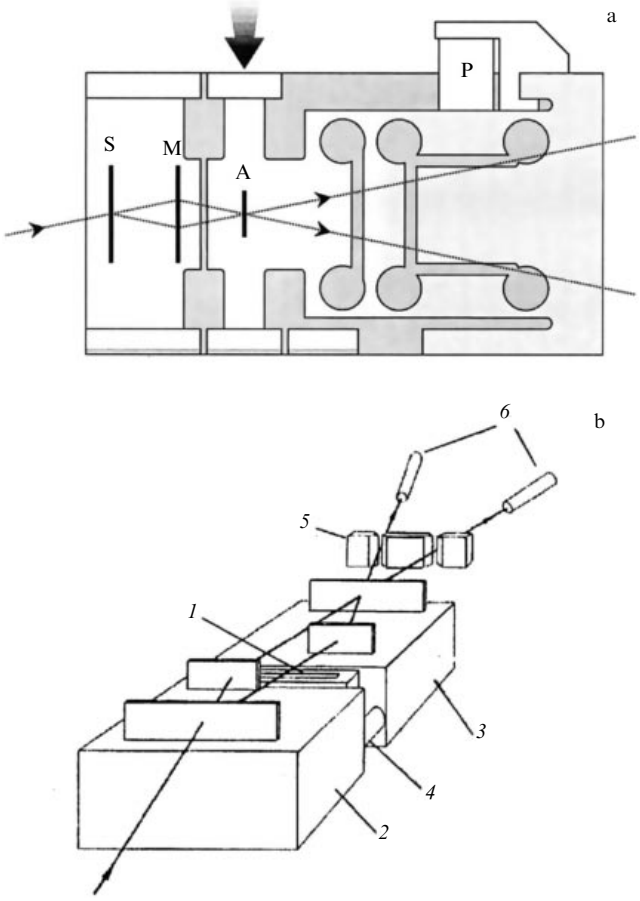

Figure 14. Layout of the X-ray interferometer with a linear scanning: the thick arrow indicates the displacement direction of the mobile interferometer unit with analyzer A; S, M — beam splitter and mirror, respectively, P — piezo driver [109]. (b) Schematic of the X-ray interferometer with angular scanning: *1* — spring connecting the immobile (*2*) and mobile (*3*) parts of the interferometer, *4* — piezo driver, *5* — slits, and *6* — detectors [113].

period $\delta\theta$ is of order 10 nrad (the authors of Ref. [113] reported intensity variations with a period of 0.002 arcsec) and only depends on the interplanar spacing d, the distance z_{AM2} between the two lamellae of the rotating block (Fig. 7b), and the thickness t_{M2} of the lamella served as a mirror:

$$\delta\theta = \frac{d}{z_{AM2} + t_{M2}} \,. \tag{21}$$

The dependence of the period $\delta\theta$ on t_{M2} is due to dynamical X-ray diffraction effects [113], unlike the result that follows from a purely geometrical consideration [111]. To achieve a good visibility of the angular moiré fringes in the entire range, the mirror lamella should be two times as thick as the beam-splitter and analyzer crystals [113]. The theoretical visibility of the fringes is 100% near the maximum of the rocking curve (RC), and not less than 50% at its falling branches [114].

The X-ray interferometer with angular scanning can be applied as a calibration tool for optical autocollimators, as well as in optical interferometry for precise measurements of angles [113].

5.2.4 Silicon lattice parameter determination. Fundamental physical constants, such as the Avogadro constant, the Planck constant to the neutron mass ratio, and the wavelengths of the characteristic X-ray spectra of atoms and gamma-quanta can be determined using silicon crystals. However, precise knowledge of its lattice parameter is needed for these purposes. The relations between fundamental constants and other clearly defined physical constants require that the Si lattice parameter be known to better than 10^{-8}.

The actual lattice parameter of very clean, almost perfect silicon samples, grown by the zone melting method, depends on the residual concentrations of carbon and oxygen impurities ($\sim 10^{15}$ cm^{-3}). This indicates the absence of significant systematic effects caused by other impurities, vacancies, or isotopes. Thus, the lattice parameters of different silicon crystals are equal between themselves within a few units of 10^{-8} after making corrections for the presence of contaminant carbon and oxygen atoms. The lattice parameter of almost perfect silicon, which is characterized by the specific concentrations of these impurities, is thus an excellent standard to measure subnanometer lengths. Reducing the carbon and oxygen impurities by one order of magnitude makes it unnecessary to introduce the contaminant-driven corrections [115–117].

The LLL-interferometer constitutes an achromatic device. This property underlies the assumption that the lattice parameter can be measured by counting the translational moiré fringes per unit length — in this case, the X-ray wavelength need not be known whatsoever.

A combination of X-ray and optical interferometers [118, 119] (Fig. 15) allowed simultaneous measurement of the X-ray and optical beam intensity during analyzer crystal displacement. Their variations have the same period as the interplanar spacing of the silicon lattice and the half-wavelength of the laser beam, respectively. Thus, the crystal analyzer displacement is measured in both X-ray and optical scales, so that the ratio $\lambda/2d$ is expressed through the ratio of the number q of X-ray periods to the number m of optical periods in a given scan [120]:

$$d = \frac{m}{q}\frac{\lambda}{2} = \frac{\lambda}{2(Q+\rho)} \,, \tag{22}$$

where Q and ρ are the integer and fractional parts of the ratio m/q, and λ is the optical laser wavelength.

To avoid counting all moiré fringes, it is sufficient to determine the fractional part ρ at the final stage of the analyzer displacement: by increasing the displacement length (paper [121] used the progression 1, 10, 100, 1000, 5000 optical periods), it is possible to gradually improve the experimental accuracy. The fractional part can be calculated based on the phase step method [122] or the quadrature signal method [123].

Equation (22) implies that the larger the crystal analyzer displacement, the higher the method accuracy. The displacement range is limited by the smoothness and linearity of the displacement within a few nanometers. In addition, it is important to maintain the 'pitch' (the turn in the analyzer plane) and 'yaw' (the turn in the diffraction plane) within a few nanoradians along the entire scanning length. It is also necessary to provide a good visibility of the moiré pattern, which requires a compromise between the opposite demands of the maximal displacement and rigidity of the interferometer construction. The construction rigidity is necessary for keeping vibrations, which degrade visibility, within a few fractions of one angström.

Progress in X-ray and optical interferometry assumes ongoing development of more powerful methods to control

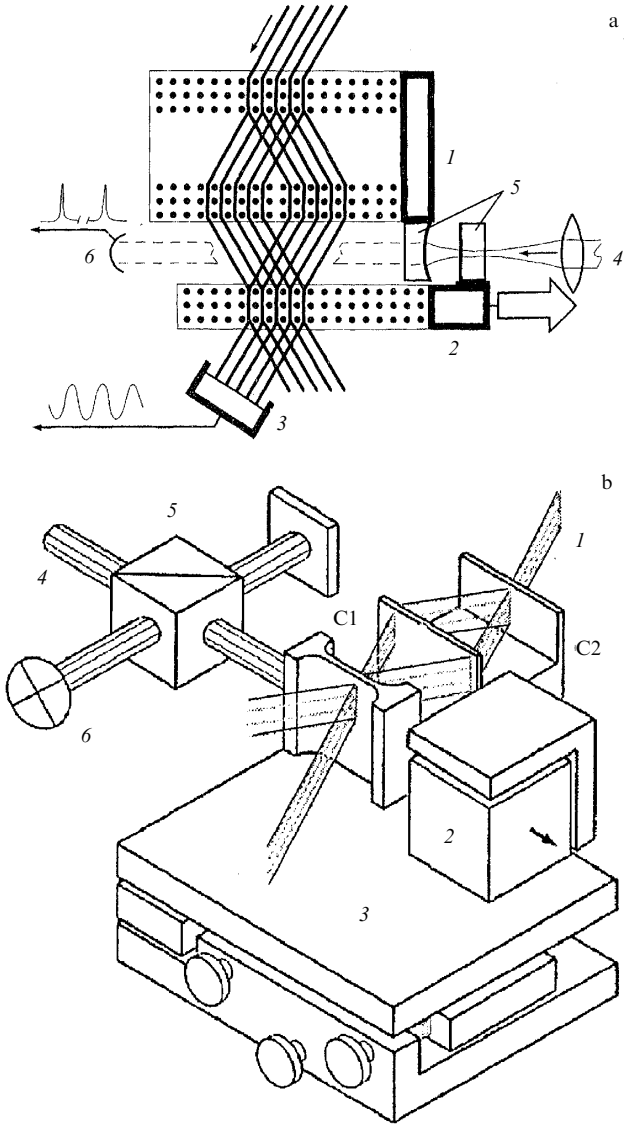

Figure 15. Layouts of X-ray optical interferometers. (a) Single-block X-ray interferometer: *1* and *2* — immobile and mobile units, respectively, *3* — X-ray detector, *4* — laser beam, *5* — mirrors forming optical Fabri–Perot interferometer, and *6* — PEM [119]. (b) Two-block X-ray interferometer: C1 — mobile block (analyzer) with mirror end surface to reflect laser beam, C2 — immobile block (beam splitter and mirror), *1* — X-ray beam, *2* — capacitive sensor (transducer), *3* — two-axial slanted platform, *4* — laser beam, *5* — optical interferometer, and *6* — position-sensitive detector [124].

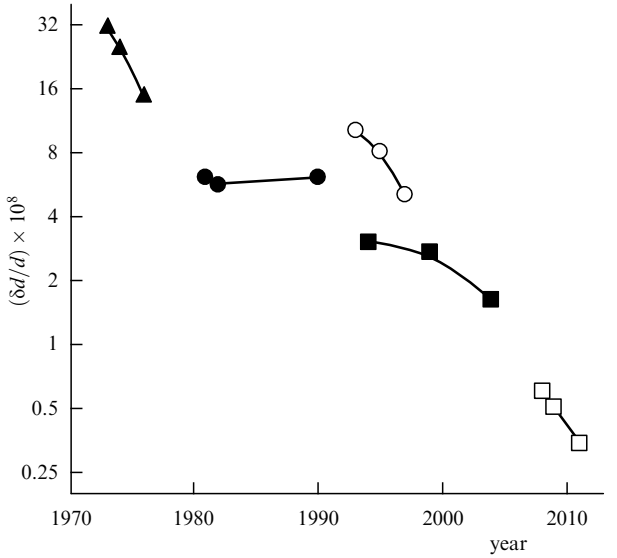

Figure 16. Decrease in calculation uncertainty of the interplanar spacing $\delta d/d$ over the last 40 years according to publications by different research groups: dark triangles — [125–127], dark circles — [128–130], light circles — [131–133], dark squares — [121, 124, 134], and light squares — [135–137].

experimental conditions more precisely, which increases the shift range and decreases parasitic rotations and transversal motions.

The broadening of the scanning range both increases the measurement accuracy and provides the opportunity of studying a wider region of the analyzer crystal, thereby controling its perfection degree, as well as measuring the real mean value of the lattice parameter. Therefore, a separated (two-block) interferometer (Fig. 15b) seems to be the most promising. Its successful performance is a difficult task: its immobile and mobile units must be adjusted in such a way that vibrations and displacements do not affect the measurement accuracy.

Let us try to follow the consecutive ameliorations of the method made by several scientific groups that participated in a sort of a scientific relay (Fig. 16), which enabled coming close to solving an important metrology problem — the creation of a new length standard. Thus

1981. 40-μm scanning range was attained [128].

1994. Scanning range was increased to 85 μm [134].

1995. A feedback system was put into operation that decreased both the pitch and yaw of the objective table to provide its rectilinear displacement inside a few nanoradians within 100 μm [132].

1997. The control system of the experiment was implemented that provides a smooth displacement of the crystal up to 2 mm with the pitch, and yaw within 1 nrad [138].

2004. A new two-axial platform with electronic control for compensation of parasitic rotations and the rectilinear crystal displacement errors was constructed. The platform can provide crystal positioning on the atomic scale [124].

2009. The scanning range was increased to 5 cm by using a guide for an L-like carriage with the mobile analyzer sliding over a quasioptical rail and an active rack with three piezoelectric 'legs' resting upon the carriage. The displacements, rotations, and parasitic transverse movements of the crystal are controlled by laser interferometry and capacitive sensors. The feedback provides picometer positioning and the adjustment of the interferometer rectilinear motion with a nanometer accuracy [136].

5.2.5 Study of structural defects in crystals. The X-ray LLL-interferometer is widely used to study both structural defects arising during the growth (dislocations [11, 139–141], growth striations [11]) and specially introduced strain fields into the analyzer lamella by ion implantation [142–145], diffusion [146] (Fig. 17), concentrated loading [147], laser irradiation [148], ultrasound [11], temperature gradient [149, 150], and electromagnetic fields [151, 152].

Hart [7] showed that the orientations and Burgers vectors of dislocations can be completely determined provided that a sufficiently large number of moiré patterns can be obtained (Fig. 18). However, even simple dislocation configurations

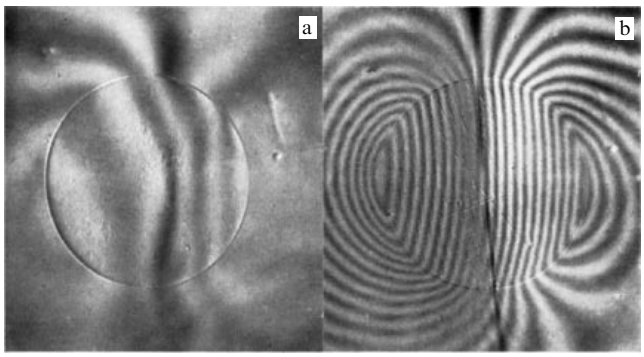

Figure 17. X-ray moiré patterns from an aluminum disc 5 mm in diameter vaporized onto the analyzer before (a) and after (b) short annealing at a temperature of 500 °C [7].

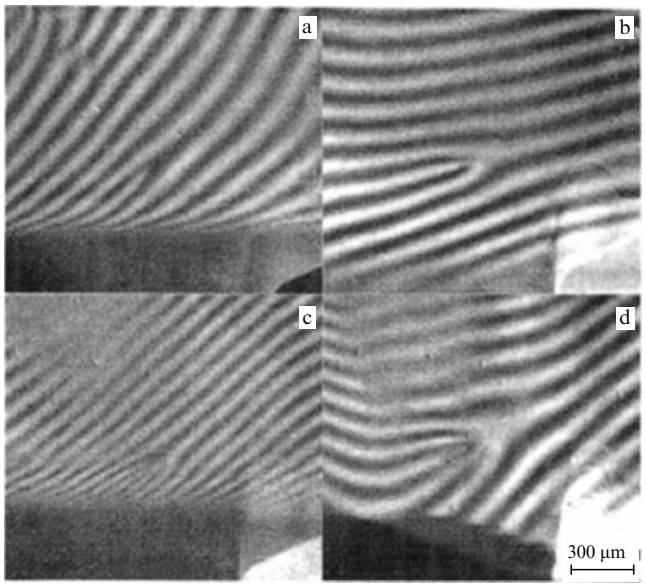

Figure 18. X-ray moiré patterns of dislocations for different reflections: (202) (a), (220) (b), (422) (c), and (440) (d); MoKα emission [7].

can produce clearly contradictory, complicated moiré patterns.

When determining the silicon lattice parameter, it is important to know how perfect the crystal lamellae of the scanning interferometer are. Paper [153] attempted to determine the strain fields in the analyzer crystal. A phase modulator (the plastic plate with a thickness of about 500 μm) was inserted between the beam splitter and mirror in such a way that both X-ray beams were overlaid in the interferometer (Fig. 19a). By turning around the phase modulator through the angle ξ, the optical paths of the beams change in counterphase: one decreases, while the other increases. A simple geometrical analysis shows that such a phase modulator of thickness T_m causes the optical path difference $2T_m(1-n)(\sin\theta_B/\cos^2\theta_B)\,\xi$, where n is the refraction index. A phase modulator overlaying both optical paths is more advantageous. First, it doubles the method sensitivity. Second, and more importantly, the optical path difference can be approximated by a linear function of ξ in the limit of small turning angles.

The interference pattern was registered by eight rows of scintillation counters with 1.5×1 mm^2 pixels. To obtain the topogram displayed in Fig. 19b, the interferometer was displaced along the x-axis with a 1-mm step. To determine the phase distribution, the intensity of the transmitted beam (O-beam) was measured at each interferometer position for 60 different angular positions of the phase modulator.

Four crystal regions of the interferometer participate in the formation of the moiré pattern; therefore, strictly speaking, the method does not provide information about the strain fields in an individual lamella out of three ones. Theoretical [154] and experimental [155] studies of the strain fields were carried out for a double-T analyzer (Fig. 15b).

5.2.6 Time-resolved interferometry. Study of nuclear resonance scattering. Pulse properties of the synchrotron radiation (SR) are employed in time-resolved interferometry. For example, a collimated beam from an SR source can be used in a crystal interferometer with unresonance component discrimination, which is not feasible with an ordinary radioisotope source. The high longitudinal coherence of nuclear resonance scattering guarantees the observation of interference between X-rays emitted by different nuclei, interference between freely induced signals separated by a time interval, and collective photon absorption and reemission.

In experiments studying nuclear resonance scattering in the forward direction, the nuclear target is usually inserted between the first and second wafers of the interferometer, and the phase shifter between the second and third wafers (Fig. 20a). The authors of paper [156] used a plane-parallel silicon wafer of thickness 290 μm as the phase shifter, and the relative phase change was due to rotation of this silicon wafer. The energy of monochromatic SR can be tuned to resonance. Figure 20b demonstrates the time spectrum of nuclear resonance scattering in the forward direction, which was obtained from a stainless foil 4 μm in thickness enriched in ^{57}Fe isotope. Experiments revealed that the phase information is passed via reemission through the intermediate nuclear resonance state. This phase information can be utilized as phase memory, which is analog, not digital, memory. It should be stressed that in these experiments the Mössbauer nuclei played the part of the resonating cavity for SR.

Paper [157] reported experimental results that successfully demonstrated interference during nuclear resonance scattering in the forward direction in two ^{57}Fe-enriched stainless foils of different thicknesses, where intensity variations in phase and counterphase were observed with an aid of different time windows of the discriminator. The use of the time delay (Fig. 20b) is justified for observing the interference between different decay-induced beams. This interference arises between X-ray beams emitted by different nuclei. Contrast interference oscillations were obtained with a visibility corresponding to that of the interferometer itself. Consequently, two beams emitted by different nuclei at different times during resonance nuclear scattering are coherent and their wave packets fully coincide in time.

When two targets with insignificantly different nuclear excitation energy levels are inserted into different optical paths of the interferometer, then, by measuring the intensity variations of one of the output beams, it is possible to determine the phase incursion caused by such differences. The time distribution of scattered photons was also measured when identical targets were inserted into both beams, with one of the targets being displaced to produce the Doppler effect [158].

Quite often, the results of nuclear resonance scattering experiments are difficult to interpret, in particular, when the

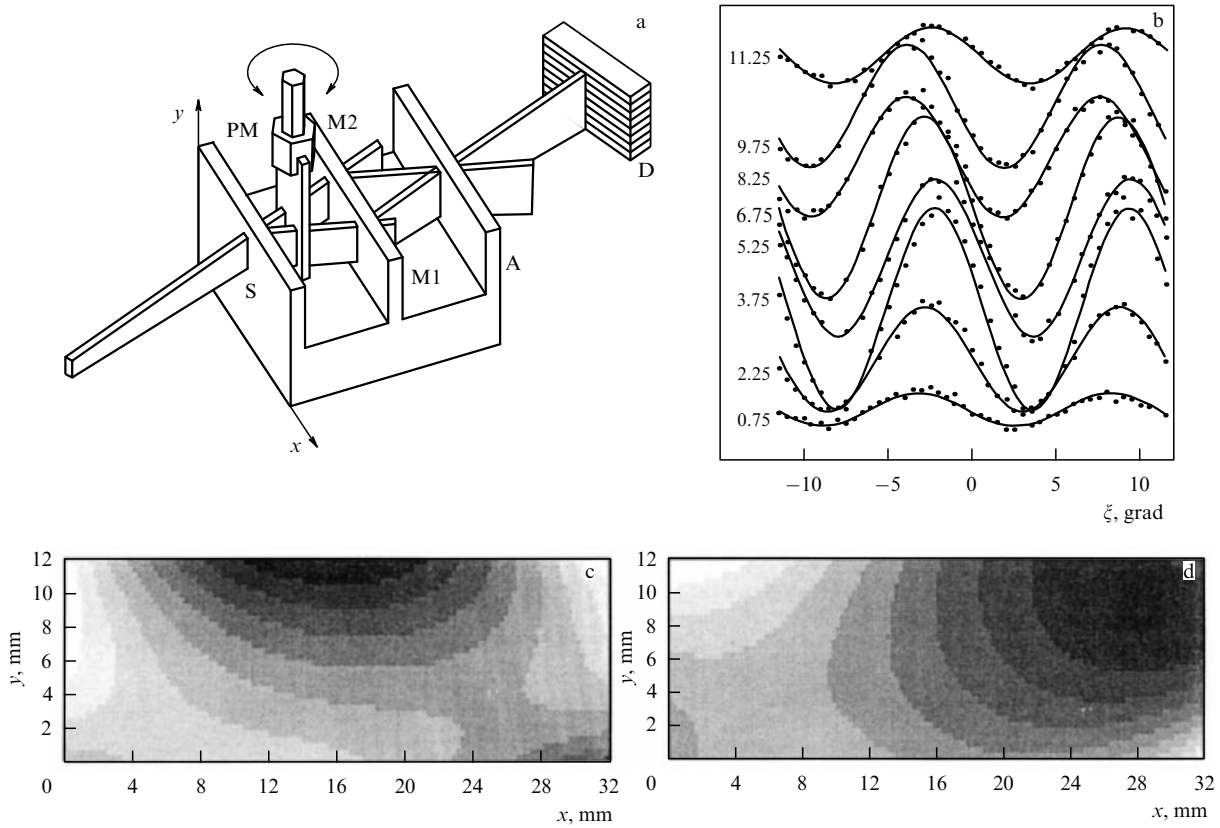

Figure 19. Experiment on determining the strain field in the LLL-interferometer. (a) The experimental layout: PM — phase modulator, D — detector, S — beam splitter, M1, M2 — mirrors, and A — analyzer. (b) The O-beam intensity as a function of the phase modulator rotation angle for an 8-pixel column. Numbers alongside the curves mark the y-coordinate of the pixel (in mm). The curves are vertically shifted for convenience. (c) Contour plot of the lattice parameter relative change. Eight equidistant levels are shown by grades of grey color from -8×10^{-9} (white) to $+16 \times 10^{-9}$ (black). (d) The contour plot of the lattice plane rotation angle. Eight equidistant levels are picked out by grades of grey color from -16 nrad (white) to -24 nrad (black) [153].

approximate positions of nuclear energy sublevels are unknown. Paper [159] made use of an X-ray interferometer with an etalon sample having sharp nuclear resonance levels to prepare an X-ray beam with a controllable phase. A sample with similar resonances was inserted into the beam outside of the interferometer. The change in the X-ray emission phase on the sample can be uniquely determined based on the time-dependent intensity at the sample output. The possibility of setting the sample outside the interferometer allows the total external X-ray reflection to be exploited, which is highly advantageous in studies of thin films or nanostructures.

5.2.7 Determination of the coherence of X-ray beams. When in an X-ray LLL-interferometer the distance (L_{SM}) between the beam splitter and the mirror differs from the distance (L_{MA}) between the mirror and the analyzer, a simple geometrical consideration shows that two beams that converge at the analyzer at one point should cross the beam-splitter plate at

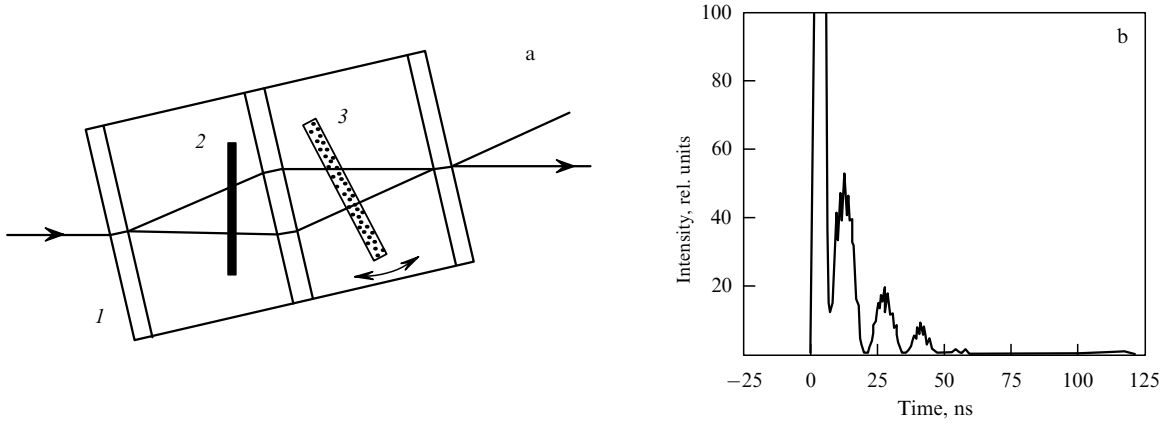

Figure 20. (a) Schematics of experiment on nuclear resonance scattering X-ray interferometry in the forward direction: *1* — LLL-interferometer, *2* — sample, and *3* — phase modulator. (b) Time spectrum of scattering; the resonance scattering corresponds to the time interval from 35 to 89 ns [156].

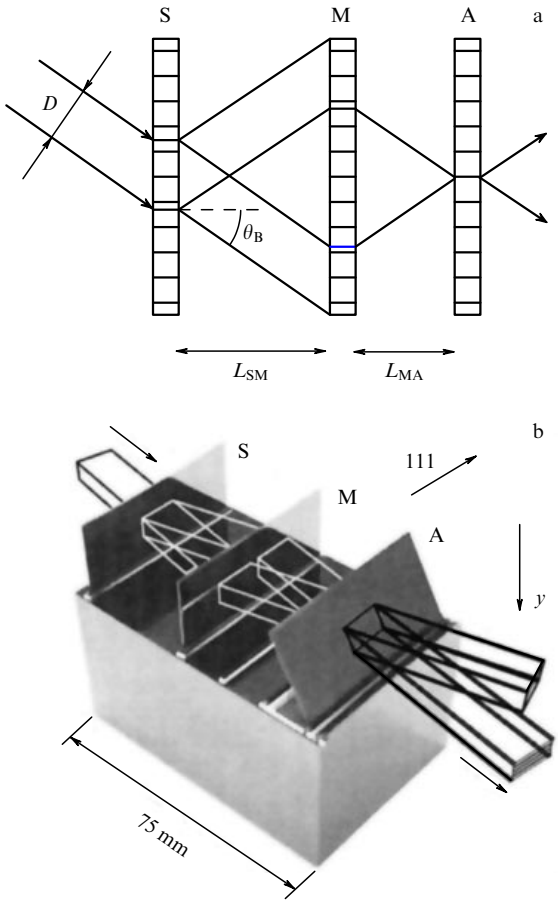

Figure 21. (a) The X-ray interferometer with different distances between the beam splitter and the mirror (L_{SM}), and between the mirror and the analyzer (L_{MA}). D is the distance between two beams converging at one point A on the analyzer [161]. (b) Exterior view of the interferometer with an inclined analyzer [160].

points separated away by the distance $D_S = D \sec\theta_B$ (Fig. 21a). The spatial separation of these beams is a function of L_{SM} and L_{MA} and vanishes when $L_{SM} = L_{MA}$ [160]:

$$D_S = 2(L_{MA} - L_{SM}) \tan\theta_B \,. \tag{23}$$

To observe the effect of the spatial separation D_S on the interference pattern visibility, the distance L_{MA} should be continuously changed. This can be realized, for example, using an inclined analyzer plate (Fig. 21b).

In an interferometer with the analyzer inclined by angle ψ to the y-axis, the interference fringes have period Δy [161]:

$$\Delta y = \frac{d}{|\Delta\theta \tan\psi|} \,, \tag{24}$$

where $\Delta\theta$ is the deviation from the exact Bragg angle.

When the image of a homogeneous and partially coherent source of size s is observed at distance z from the source, the coherence function $\gamma(D)$ is given by the formula [161]

$$\gamma(D) = \frac{\sin(\pi\omega\lambda^{-1}D)}{\pi\omega\lambda^{-1}D} \,, \tag{25}$$

where $\omega = s/z$.

An interferometer with an inclined analyzer can be used to determine the transverse coherence of the primary beam from the interference fringe visibility given by expressions (9) and (25).

The longitudinal coherence might be determined with the aid of a Michelson interferometer.

6. Michelson X-ray interferometers

By a Michelson interferometer is usually meant one capable of producing a broad range of observing interference maxima in a wide spectral range. This feature makes the instrument particularly useful for precision measurements and for Fourier spectroscopy, which is even more important [162].

Michelson interferometers for visible light have existed for more than a century. In these instruments, the primary beam is split into two: one beam with a fixed optical path length, and the other beam with a variable length. These two beams are then converged again to observe interference. The change in the interference intensity as a function of the path difference will be observed as long as the path difference is no more than the longitudinal (time) coherence length.

Generally, it is rather difficult to construct the optical setup for an X-ray interferometer which would be capable of providing a significant difference in the geometrical paths of two beams without strongly violating the focusing condition, which requires that any pair of interfering X-rays coming out from one point of the source meet at one point on the analyzer.

The X-ray interferometer is ideally suited for observations of large longitudinally consistent wave packets. However, it is rather difficult to construct such an interferometer with a large X-ray path difference.

Despite the existing opinion [163] that LLL-interferometers, while being capable of providing a large number of interference orders, are not suited to produce a desired path difference between the beams, the authors of Ref. [164] proposed a setup of an X-ray interferometer with wedgelike lamellae (Fig. 22a) providing the path difference Δ between the interfering beams:

$$\Delta = L \tan\alpha_1 (\sec\theta_B - 1) \,, \tag{26}$$

where α_1 is the angle of the mirror wedge, and L is the distance from the X-ray beam point of incidence at the second lamella (mirror) to the wedge base.

Having determined the value of the parameter L, at which the interference pattern disappears during the interferometer displacement relative to the primary beam parallel to the diffraction vector, one can calculate the longitudinal coherence length of the primary beam using formula (26).

To provide beam focusing, the analyzer lamella wedge angle α_2 should be determined by the mirror wedge angle and the Bragg angle:

$$\tan\alpha_2 = \frac{\tan\alpha_1}{2 - \tan\theta_B \tan\alpha_1} \,. \tag{27}$$

This condition implies that the interferometer should be designed for a particular energy of the beam. In addition, geometrical condition (7) is violated here, which can disprove the interference pattern quality.

In paper [165], a setup of a chromatic X-ray BBBB-interferometer (Fig. 6a) with a large and variable path difference was proposed, which was successfully realized later in Ref. [166]. It can be exploited for precise measurements of the X-ray beam coherence, as well as in X-ray

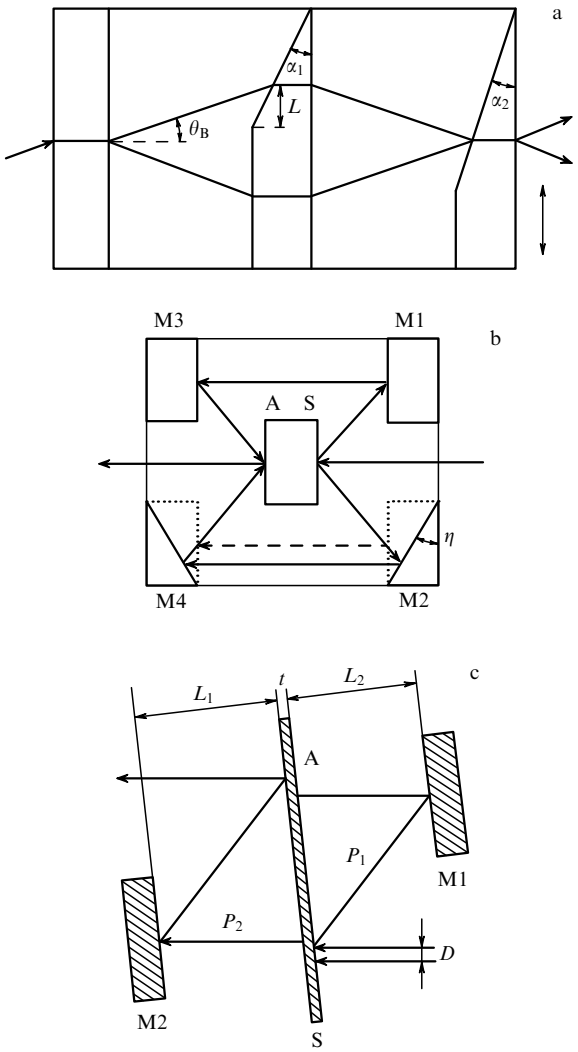

Figure 22. Optical layouts of X-ray (a) LLL- [164]; (b) BBBB- [165, 166], and (c) Michelson BBB-interferometers [156, 168] (see text).

Fourier spectroscopy. To provide the path difference between the two beams, the mirror surfaces (M2 and M4 in Fig. 22b) are inclined by small angle η to the surfaces of another pair of mirrors (M1 and M3). Thus, the change in the path difference Δ depends on the displacement D of the primary beam along the beam-splitter surface [167]:

$$\Delta = \frac{2D \tan\eta\left[1 + \sin(\theta_B - \varphi)\right]}{\sin(\theta_B - \varphi)}\,, \tag{28}$$

where φ is the angle between the crystal surface and the reflecting planes.

A small skew at 1° changes the asymmetry factor by 4% and insignificantly affects the location and intensity of the diffraction peak. Indeed, this causes very little angular changes in the beam location (~ 1 mrad), which lead to a small horizontal shift (defocusing) on the analyzer surface: 70 nm for reflections Si(440)/Si(404) (for Si(880)/Si(808) reflections, the horizontal shift is about one fourth the size). This small change can be neglected, and this will not affect the interference pattern visibility.

In this setup, a path difference as large as 1 mm is attainable. It is limited only by the size of the silicon crystal available. A larger 'slant' of mirrors M2, M4 also increases the path difference. Here, the interferometer adjustment is relatively simple, but such an interferometer is suitable for studies of a small number of interference orders. In addition, the usage of multiwave diffraction restricts applications of this type of a Michelson interferometer by discrete values of the primary beam energy, at which the interferometer's pass band is only a few millielectron-volts.

To study nuclear resonance scattering, papers [156, 168] took advantage of a BBB-interferometer (Fig. 5c) in which the optical path difference was 2.4 mm, which is a record for instruments described in the literature. This is much larger than the SR longitudinal coherence length, but much smaller than the nuclear resonance scattering length on ^{57}Fe. The layout of a BBB-interferometer with a large optical path difference is presented in Fig. 22c. The crystal plate AS serves as the beam splitter and analyzer. The plates M1 and M2 are utilized as mirrors. The symmetric Bragg reflection Si(880) with the asymmetry parameter $b = 0.69$ for the ^{57}Fe resonance energy ($\lambda = 0.86$ Å) was used. The distances L_1 and L_2 between M1, M2 and AS were 21.65 mm and 23.35 mm, respectively, and the width t measured 1.1 mm. The optical path difference Δ is given as follows:

$$\Delta = (L_2 - L_1)\left[\frac{1}{\sin(\theta_B - \varphi)} + \frac{1}{\sin(\theta_B + \varphi)}\right]. \tag{29}$$

Clearly, the distance D between the input beams, which converge at one point in the output, should be smaller than the transverse coherence length l_x of the primary beam:

$$D = (L_2 - L_1)\left[\cot(\theta_B - \varphi) + \cot(\theta_B + \varphi)\right] \times \sin(\theta_B + \varphi) < l_x\,. \tag{30}$$

The authors of Refs [156, 169, 170] improved the setup of the Michelson BBB-interferometer: one of its mirrors was joined to the crystal base by a series of elastic connections in such a way that a piezo driver could displace this mirror perpendicular to other units of the interferometer, thus providing a variable X-ray path difference. In addition, the main BBB-interferometer could be used as an auxiliary LLL-interferometer for preliminary testing of the structural perfection of the Michelson interferometer.

From the scientific point of view, it would be very desirable to make Fourier spectroscopy operable in the hard X-ray range. Then, SR spectra could be measured, including those transformed by ondulators and wigglers, as could the spectra of free electron lasers. The setups of the Michelson interferometers considered here can provide a path difference in the mm range. This can be sufficient, for example, to analyze the longitudinal coherence of radiation, but insufficient for measuring the full radiation spectrum by means of Fourier spectroscopy.

The Michelson interferometer setup proposed by Appel and Bonse [171] provides the spectral resolution needed for Fourier spectroscopy. It utilizes an LLL-interferometer, together with two Bragg grooved crystals B1, B2 (one monoblock per branch of the interference loop) connected by a thin elastic bridge E (Fig. 23). These blocks are inserted into the gaps of the LLL-interferometer and can rotate relative to each other to produce the optical path difference between the two interfering beams. This is a distinctive feature of this optical setup from those considered above, in which the linear displacements of the entire interferometer or its separate units are used to produce the path difference.

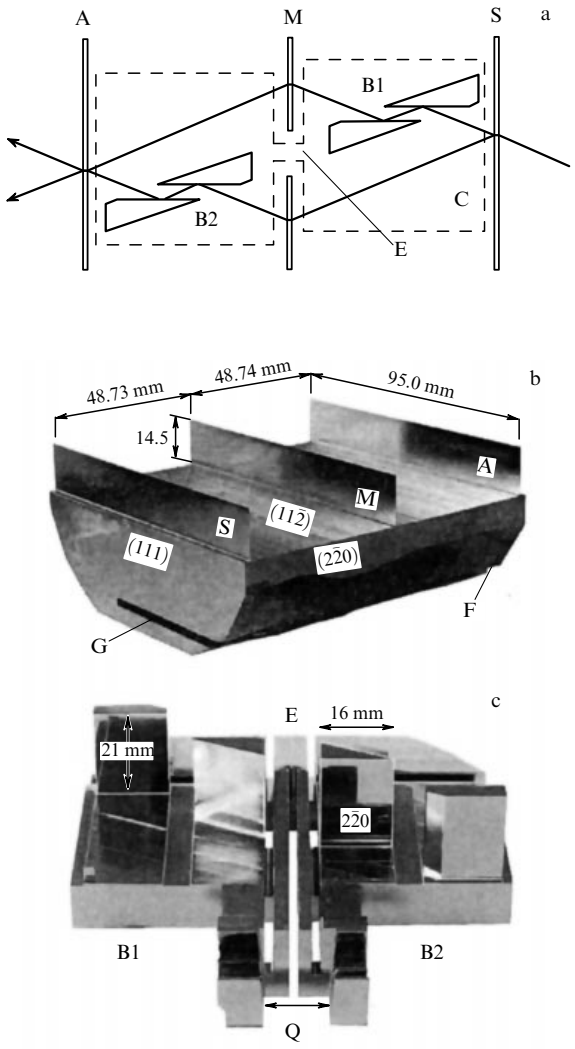

Figure 23. Optical layout (a), sizes and orientations of the LLL-interferometer (b) and optical unit C with a pair of single-unit grooved Bragg crystals B1, B2 (c): S — beam splitter, M — mirror, A — analyzer, E — elastic bridge for the relative adjusting of B1 and B2, G — slot to decrease elastic tensions in the base F, and Q — adjusting gap for piezo driver.

It is essential that the rotation of Bragg crystals B1, B2 through their RC range change each beam propagation direction inside the crystals, not outside, so that the reflection condition in the LLL-interferometer remains to be fulfilled. Such a rotation causes the path difference Δ of two beams yielding the phase shift $\Phi = 2\pi\Delta/\lambda$. The path difference Δ depends on the Bragg angle, the width of slots (grooves) D_1 and D_2, the angle φ, and angular deviations β_1, β_2 of the beams from the RC center for the Bragg nanoblocks [38]. For a simplified case of the symmetrical diffraction ($\varphi = 0$) and when $D_1 = D_2 = D$, one obtains

$$\Delta = 2D\Delta\beta\cos\theta_B\,, \tag{31}$$

where $\Delta\beta = \beta_1 - \beta_2$. The path difference arises if $\Delta\beta \neq 0$. By setting $D = 2$ mm and $\lambda = 1.54$ Å (CuKα), the path difference for $\Delta\beta_{min} = 8.7 \times 10^{-3}$ arcsec (4.2×10^{-8} rad) is equal to λ, which allows one to obtain about 800 interference orders before the grooved crystals move out of the reflecting position. Here, the spectral resolution $\Delta\lambda/\lambda$ should be determined by the formulas

$$\frac{\Delta\lambda}{\lambda} = \Delta\beta_{min}\cot\theta_B = \frac{\lambda}{2D\sin\theta_B} = \frac{d}{D} = \frac{1}{N_d}\,, \tag{32}$$

where N_d is the number of reflecting planes accommodated in the Bragg crystal gap.

At $d = 1.92$ Å [reflection (220)] and $D = 2$ mm, the spectral resolution $\Delta\lambda/\lambda$ should be on the order of 10^{-7}. Therefore, with such an interferometer, interference maxima can be analyzed in detail, but the exploitation of the two separate crystal monoblocks makes the preliminary adjustment more difficult; moreover, this instrument is more susceptible to temperature and vibrational stability than a single monoblock interferometer.

A feature of the optical layout under discussion is that by 'mixing' the Laue and Bragg diffractions a significant optical path difference can be obtained without noticeable defocusing. The defocusing Δz reduces the interference pattern contrast and, hence, narrows the maximum scanning range $\Delta\beta_{max}$ and the spectral resolution $\Delta\lambda/\lambda$ of the interferometer. Clearly, the defocusing increases proportionally to the interference order M [163]:

$$\Delta z = D\Delta\beta = \frac{\lambda M}{2\cos\theta_B}\,. \tag{33}$$

For $M_{max} = 40{,}000$, the defocusing amounts to $\Delta z = 3.2$ μm, which is sufficiently small to significantly affect the contrast. On the other hand, taking into account the limits on the manufacturing of interferometer units, certain strict conditions must be fulfilled: to sustain a high contrast, changes in the slot width D and in the position and planeness of wafers in the LLL-interferometer should be within 3 μm [163].

7. Conclusions

As we have explained above, X-ray interferometers can be employed to measure the extremely small lattice deformations of almost perfect crystals, the X-ray refraction coefficient to within 0.1%, and the coherence length of X-ray beams, and can be used for the X-ray phase-contrast microscopy of, for example, biological objects.

Combined interferometers or interferometers allowing large translational displacements of the crystal open up a new avenue in subnanometer metrology and in absolute measurements of fundamental physical constants. This new possibility enables high-precision absolute measurements of lengths in the region where up to now such measurements have been made using a light standard with a finite spectral width, which introduced additional measurement uncertainties.

The X-ray interferometer, which is sometimes referred to as the 'angström ruler', is an ideal instrument for high-precision measurements. Such measurements are increasingly required in different fields of science and technology, including microelectronics, visible light optics, optical information carriers, calibration of high-resolution shift transducers, and scanning acoustic and atomic-force microscopes. The X-ray interferometer provides a very precise scale for such a calibration in the subnanometer range. The instrument uses the silicon lattice parameter as the well-determined scale that is directly related to the length standard.

The future of X-ray interferometry, apparently, is related to the capability of precisely manufacturing the crystal X-ray optics elements, as well as to the mutual adjustment and

positioning of separate interferometer units. The extension of the scanning range of the analyzer crystal to several centimeters is one of the problems. Such an extension should rely on integration of control over six degrees of freedom for its displacement and the laser metrology.

Obtaining a large variable path difference of interfering coherent beams is another problem. Its solution would provide the possibility of constructing X-ray equivalents of the Michelson interferometer with taking aim at the experimental realization of Fourier spectroscopy.

The moiré pattern is very sensitive to tiny phase gradients. Therefore, of all known X-ray phase-contrast image methods [172], crystal interferometry is the most sensitive to small local density variations in the sample under study. This method directly reveals the phase change, whereas other methods are sensitive to first and second phase derivatives. The possibility of industrial production of bulky silicon crystal boules with a perfect structure can return crystal interferometry to the leading position in phase-contrast imaging. The growth of silicon crystals with the reduced amount of impurities ($< 10^{14}$ cm^{-3}) can make this material a new length etalon.

References

1. Chikawa J *Appl. Phys. Lett.* **7** 193 (1965)
2. Lang A R, Miuscov V F *Appl. Phys. Lett.* **7** 214 (1965)
3. Bonse U, Hart M *Appl. Phys. Lett.* **6** 155 (1965)
4. Bonse U, Hart M *Appl. Phys. Lett.* **7** 99 (1965)
5. Hart M *J. Phys. D Appl. Phys.* **1** 1405 (1968)
6. Hart M, Bonse U *Phys. Today* **23** (8) 26 (1970)
7. Hart M *Rep. Prog. Phys.* **34** 435 (1971)
8. Hart M *Proc. R. Soc. Lond. A* **346** 1 (1975)
9. Hart M *Nucl. Instrum. Meth.* **172** 209 (1980)
10. Siddons D P *AIP Conf. Proc.* **75** 236 (1981)
11. Raransky M D et al. *Proc. SPIE* **2647** 457 (1995)
12. Il'in V N, Kobets N A, Leshkov S V *J. Appl. Spectrosc.* **66** 481 (1999); *Zh. Priklad. Spektrosk.* **66** 451 (1999)
13. Mana G *Proc. SPIE* **4900** 257 (2002)
14. Momose A J *Synchrotron Radiat.* **9** 136 (2002)
15. Stecher M *Am. J. Phys.* **32** 247 (1964)
16. Miuscov V F, in *Problemy Sovremennoi Kristallografii. Sb. Pamyati A V Shubnikova* (Problems of Modern Crystallography. In memory of A V Shubnikov) (Exec. Eds B K Vainshtein, A A Chernov) (Moscow: Nauka, 1975) p. 186
17. Pinsker Z G, in *Problemy Sovremennoi Kristallografii. Sb. Pamyati A V Shubnikova* (Problems of Modern Crystallography. In memory of A V Shubnikov) (Exec. Eds B K Vainshtein, A A Chernov) (Moscow: Nauka, 1975) p. 172
18. Authier A, Milne A D, Sauvage M *Phys. Status Solidi B* **26** 469 (1968)
19. Tanemura S, Lang A R *Z. Naturforsch. A* **28** 668 (1973)
20. Ohler M, Härtwig J *Acta Cryst. A* **55** 413 (1999)
21. Simon D, Authier A *Acta Cryst. A* **24** 527 (1968)
22. Aboyan A O et al. *Cryst. Res. Technol.* **25** 1405 (1990)
23. Hart M, Milne A D *Acta Cryst. A* **26** 223 (1970)
24. Bezirganyan P Kh, Drmeyan Kh R, Aladzhadzhyan G M *Phys. Status Solidi A* **54** 729 (1979)
25. Bonse U, Hart M, Schwuttke G H *Phys. Status Solidi B* **33** 361 (1969)
26. Fedorov A A et al. *J. Phys. D Appl. Phys.* **36** A44 (2003)
27. Khokhar R U, Haneman D *J. Appl. Phys.* **43** 317 (1972)
28. Chu X, Tanner B K *Mater. Lett.* **5** 153 (1987)
29. Drmeyan H R *Acta Cryst. A* **60** 521 (2004)
30. Ohler M, Prieur E, Härtwig J *J. Appl. Cryst.* **29** 568 (1996)
31. Ohler M, Köhler S, Härtwig J *Acta Cryst. A* **55** 423 (1999)
32. Ohler M, Härtwig J, Prieur E *Acta Cryst. A* **53** 199 (1997)
33. Yoshimura J *Acta Cryst. A* **52** 312 (1996)
34. Pinsker Z G *Dinamicheskoe Rasseyanie Rentgenovskikh Luchei v Ideal'nykh Kristallakh* (Dynamical Scattering of X-Rays in Perfect Crystals) (Moscow: Nauka, 1974)
35. Bonse U, Hart M *Phys. Status Solidi B* **33** 351 (1969)
36. Lang A R *Nature* **220** 652 (1968)
37. Brádler J, Lang A R *Acta Cryst. A* **24** 246 (1968)
38. Bonse U et al. *Metrologia* **31** 195 (1994)
39. Besirganyan P A, Eiramdshyan F O, Truni K G *Phys. Status Solidi A* **20** 611 (1973)
40. Heinrich M, Petrascheck D, Rauch H *Z. Phys. B* **72** 357 (1988)
41. Bonse U, Hart M *Z. Phys.* **194** 1 (1966)
42. Bonse U, Hart M *Acta Cryst. A* **24** 240 (1968)
43. Würges J et al. *J. Appl. Cryst.* **32** 1152 (1999)
44. Koyama I, Yoshikawa H, Momose A *Jpn. J. Appl. Phys.* **42** L80 (2003)
45. Izumi K et al. *Jpn. J. Appl. Phys.* **34** 5862 (1995)
46. Sutter J P et al. *J. Synchrotron Radiat.* **11** 378 (2004)
47. Spieker P, Bonse U *Acta Cryst. A* **34** S238 (1978)
48. Graeff W, Bonse U *Z. Phys. B* **27** 19 (1977)
49. Besirganyan P A, Gabrielyan R Z, Eiramshyan F O *Phys. Status Solidi A* **43** K183 (1977)
50. Yoneyama A, Momose A, Koyama I *Jpn. J. Appl. Phys.* **41** L161 (2002)
51. Fezzaa K, Lee W-K *AIP Conf. Proc.* **521** 167 (2000)
52. Bonse U, Hart M *Z. Phys.* **188** 154 (1965)
53. Petrascheck D, Folk R *Phys. Status Solidi A* **36** 147 (1976)
54. Bauspiess W, Bonse U, Graeff W *J. Appl. Cryst.* **9** 68 (1976)
55. Colella R *Acta Cryst. A* **44** 1055 (1988)
56. Shulakov E V, Aristov V V *Acta Cryst. A* **35** 201 (1979)
57. Bonse U, te Kaat E *Z. Phys.* **243** 14 (1971)
58. Trouni K G, Arutyunyan L A *Phys. Status Solidi A* **92** 369 (1985)
59. Bonse U *Physica B+C* **151** 7 (1988)
60. Aladzhadzhyan G M et al. *Phys. Status Solidi A* **58** 651 (1980)
61. Aladzhadzhyan G M, Kocharyan A K, Trouni K G *Kristallografiya* **21** 1135 (1979)
62. Bezirganyan P H, Aslanyan V G, Bezirganyan S E *Phys. Status Solidi A* **110** 359 (1988)
63. Bezirganyan P A et al. *Phys. Status Solidi A* **104** 549 (1987)
64. Bagdasaryan R I et al. *Sov. Phys. J.* **27** 259 (1984); *Izv. Vyssh. Uchebn. Zaved. Fiz.* (4) 8 (1984)
65. Bonse U, Hart M *Z. Phys.* **190** 455 (1966)
66. Blokhin M A *Fizika Rentgenovskikh Luchei* (Physics of X-Rays) 2nd ed. (Moscow: GITTL, 1957)
67. Wu X, Dean A, Liu H, in *Biomedical Photonics Handbook* (Ed. T Vo-Dinh) (Boca Raton, Fla.: CRC Press, 2003) p. 26
68. Takeda T et al. *Circulation* **105** 1708 (2002)
69. Takeda M et al. *Int. J. Cardiovascular Imaging* **28** 1181 (2012)
70. Takeda T et al. *J. Synchrotron Radiat.* **19** 252 (2012)
71. Takeda T et al. *Radiology* **214** 298 (2000)
72. Takeda T et al. *Acad. Radiol.* **2** 799 (1995)
73. Takeda T et al. *Jpn. J. Appl. Phys.* **43** 5652 (2004)
74. Beckmann F, Heise K, Kölsch B *Biophys J.* **76** 98 (1999)
75. Noda-Saita K et al. *Neuroscience* **138** 1205 (2006)
76. Bruning J H et al. *Appl. Opt.* **13** 2693 (1974)
77. Momose A, Hirano K *Jpn. J. Appl. Phys.* **38** (Suppl. 38-1) 625 (1999)
78. Momose A, Takeda T, Itai Y *Radiology* **217** 593 (2000)
79. Judge T R, Bryanston-Cross P J *Opt. Lasers Eng.* **21** 199 (1994)
80. Takeda M, Ina H, Kobayashi S *J. Opt. Soc. Am.* **72** 156 (1982)
81. Momose A, Fukuda J *Med. Phys.* **22** 375 (1995)
82. Chetwynd D G et al. *Nanotechnology* **9** 125 (1998)
83. Momose A et al. *J. Physique IV* **104** 599 (2003)
84. Momose A et al. *Nucl. Instrum. Meth. Phys. Res. A* **467–468** 917 (2001)
85. Yoneyama A et al. *Nucl. Instrum. Meth. Phys. Res. A* **523** 217 (2004)
86. Momose A, Yoneyama A, Hirano K *J. Synchrotron Radiat.* **4** 311 (1997)
87. Momose A, Takeda T, Itai Y *Rev. Sci. Instrum.* **66** 1434 (1995)
88. Momose A *Nucl. Instrum. Meth. Phys. Res. A* **352** 622 (1995)
89. Momose A *Opt. Exp.* **11** 2303 (2003)
90. Begum R et al. *Acta Cryst. A* **42** 456 (1986)
91. Creagh D C *Aust. J. Phys.* **38** 371 (1985)
92. Creagh D C, Hart M *Phys. Status Solidi B* **37** 753 (1970)
93. Creagh D C *Aust. J. Phys.* **28** 543 (1975)
94. Bonse U, Materlik G *Z. Phys.* **253** 232 (1972)
95. Bonse U, Materlik G *Z. Phys. B* **24** 189 (1976)
96. Bonse U et al. *Nucl. Instrum. Meth.* **172** 223 (1980)

97. Bonse U, Hartmann-Lotsch I, Lotsch H *Nucl. Instrum. Meth. Phys. Res.* **208** 603 (1983)
98. Cusatis C, Hart M *Proc. R. Soc. Lond. A* **354** 291 (1977)
99. Hart M, Siddons D P *Proc. R. Soc. Lond. A* **376** 465 (1980)
100. Bonse U, Lotsch H, Henning A *J. X-Ray Sci. Technol.* **1** 107 (1989)
101. Bowen D K et al. *Precision Eng.* **12** 165 (1990)
102. Chetwynd D G, Siddons D P, Bowen D K *J. Phys. E Sci. Instrum.* **16** 871 (1983)
103. Bowen D K, Chetwynd D G, Davies S T *Proc. SPIE* **563** 412 (1985)
104. Becker P, Seyfried P *Proc. SPIE* **1015** 124 (1989)
105. Yacoot A, Downs M J *Meas. Sci. Technol.* **11** 1126 (2000)
106. Yacoot A, Cross N *Meas. Sci. Technol.* **14** 148 (2003)
107. Lin W et al. *Nanotechnology* **10** 412 (1999)
108. Lin W et al. *Appl. Opt.* **39** 4535 (2000)
109. Yacoot A et al. *Meas. Sci. Technol.* **12** 1660 (2001)
110. Park J, Lee M-Y, Lee D-Y *Microsyst. Technol.* **15** 1879 (2009)
111. Becker P, Bonse U *J. Appl. Cryst.* **7** 593 (1974)
112. Becker P, Stümpel J *Metrologia* **27** 127 (1990)
113. Windisch D, Becker P *J. Appl. Cryst.* **25** 377 (1992)
114. Kuetgens U, Becker P *Meas. Sci. Technol.* **9** 1072 (1998)
115. Becker P, Mana G *Metrologia* **31** 203 (1994)
116. Deslattes R D et al. *IEEE Trans. Instrum. Meas.* **36** 166 (1987)
117. Martin J et al. *Metrologia* **35** 811 (1998)
118. Deslattes R D *Appl. Phys. Lett.* **15** 386 (1969)
119. Deslattes R D, Henins A *Phys. Rev. Lett.* **31** 972 (1973)
120. Basile G et al. *IEEE Trans. Instrum. Meas.* **38** 210 (1989)
121. Bergamin A et al. *Eur. Phys. J. B* **9** 225 (1999)
122. Schwarzenberger D R, Chetwynd D G, Bowen D K *J. X-Ray Sci. Technol.* **1** 134 (1989)
123. Yacoot A, Kuetgens U *Meas. Sci. Technol.* **23** 074003 (2012)
124. Cavagnero G et al. *Metrologia* **41** 56 (2004)
125. Deslattes R D, Henins A *Phys. Rev. Lett.* **31** 972 (1973)
126. Deslattes R D et al. *Phys. Rev. Lett.* **33** 463 (1974)
127. Deslattes R D et al. *Phys. Rev. Lett.* **36** 898 (1976)
128. Becker P et al. *Phys. Rev. Lett.* **46** 1540 (1981)
129. Becker P, Scyfried P, Siegert H *Z. Phys. B* **48** 17 (1982)
130. Windisch D, Becker P *Phys. Status Solidi A* **118** 379 (1990)
131. Nakayama K et al. *IEEE Trans. Instrum. Meas.* **42** 401 (1993)
132. Fujimoto H et al. *Jpn. J. Appl. Phys.* **34** 5065 (1995)
133. Nakayama K, Fujimoto H *IEEE Trans. Instrum. Meas.* **46** 580 (1997)
134. Basile G et al. *Phys. Rev. Lett.* **72** 3133 (1994)
135. Ferroglio L, Mana G, Massa E *Opt. Express* **16** 16877 (2008)
136. Massa E, Mana G, Kuetgens U *Metrologia* **46** 249 (2009)
137. Massa E et al. *Metrologia* **48** S37 (2011)
138. Bergamin A et al. *IEEE Trans. Instrum. Meas.* **46** 576 (1997)
139. Hart M *Phil. Mag.* **26** 821 (1972)
140. Christiansen G, Gerward L, Andersen A L *J. Appl. Cryst.* **4** 370 (1971)
141. Aboyan A O et al. *Phys. Status Solidi A* **118** 11 (1990)
142. Gerward L, Christiansen G, Lindegaard-Andersen A *Phys. Lett. A* **39** 63 (1972)
143. Gerward L *Z. Phys.* **259** 313 (1973)
144. Drmeyan H R *J. Appl. Cryst.* **37** 585 (2004)
145. Drmeyan H, Aboyan A, Eyramjyan F *J. Surf. Investigat. X-Ray, Synchrotron, Neutron Tech.* **5** 155 (2011); *Poverkhnost Rentgen. Sinkhrotron. Neitron. Issled.* (2) 57 (2011)
146. Aboyan A O, Sarafyan M A *Cryst. Res. Technol.* **29** 253 (1994)
147. Fodchuk I M et al. *Proc. SPIE* **8338** 833819 (2011)
148. Shafranyuk V P *Thermoelektrichestvo* (1) 46 (2003)
149. Hart M, Sauvage M, Siddons D P *Acta Cryst. A* **36** 947 (1980)
150. Drmeyan H R *Crystallogr. Rep.* **50** 363 (2005); *Kristallogr.* **50** 407 (2005)
151. Arshakyan E Z, Aboyan A O, Bezirganyan P A *Phys. Status Solidi A* **106** 41 (1988)
152. Aboyan A O, Aghbalyan S G *Cryst. Res. Technol.* **45** 140 (2010)
153. Bergamin A et al. *J. Phys. D Appl. Phys.* **33** 2678 (2000)
154. Bergamin A et al. *Rev. Sci. Instrum.* **71** 1716 (2000)
155. Mana G, Massa E, Ferroglio L *Opt. Express* **17** 11172 (2009)
156. Hasegawa Y, Kikuta S *Hyperfine Interact.* **123–124** 721 (1999)
157. Hasegawa Y et al. *Phys. Rev. B* **50** 17748(R) (1994)
158. Izumi K et al. *Jpn. J. Appl. Phys.* **34** 4258 (1995)
159. Sturhahn W, Lábbé C, Toellner T S *Europhys. Lett.* **66** 506 (2004)
160. Yamazaki H, Ishikawa T *J. Appl. Cryst.* **36** 213 (2003)
161. Yamazaki H, Ishikawa T *Proc. SPIE* **2856** 279 (1996)
162. Bell R J *Introductory Fourier Transform Spectroscopy* (New York: Academic Press, 1972); Translated into Russian: *Vvedenie v Fourier-Spektroskopiyu* (Moscow: Mir, 1975)
163. Nusshardt M, Bonse U *J. Appl. Cryst.* **36** 269 (2003)
164. Aboyan A O, Bezirganyan P A, Eiramdzhyan F O *Dokl. Akad. Nauk Armenian SSR* **59** 245 (1974)
165. Bezirganyan P A *Phys. Status Solidi A* **40** K77 (1977)
166. Fezzaa K, Lee W-K *J. Appl. Cryst.* **34** 166 (2001)
167. Bonse U, Graeff W *Phys. Status Solidi A* **44** K131 (1977)
168. Izumi K et al. *Jpn. J. Appl. Phys.* **34** 5862 (1995)
169. Sutter J P et al. *J. Appl. Cryst.* **36** 1432 (2003)
170. Sutter J P et al. *J. Synchrotron Radiat.* **11** 378 (2004)
171. Appel A, Bonse U *Phys. Rev. Lett.* **67** 1673 (1991)
172. Lider V V, Kovalchuk M V *Crystallogr. Rep.* **58** 769 (2013); *Kristallogr.* **58** 764 (2013)